International Journal of Fatigue 201 (2025) 109181

Contents lists available at ScienceDirect

International Journal of Fatigue

journal homepage: www.elsevier.com/locate/ijfatigue

Multiscale modelling of additively manufactured Ti-6Al-4V alloy: Fatigue performance evaluation from material to structural level

Weiqian Chi [a], Wenjing Wang [a], Hongchang Zhou [b,*], Ruiguo Yan [c,*], Yoshiki Mikami [b]

[a] Key Laboratory of Vehicle Advanced Manufacturing, Measuring and Control Technology (Beijing Jiaotong University), Ministry of Education, Beijing 100044, China
[b] Joining and Welding Research Institute, The University of Osaka, Osaka 567-0047, Japan
[c] Department of Engineering Mechanics, Tsinghua University, 100084 Beijing, China

ARTICLE INFO

Keywords:
Titanium alloy
Hot Isostatic Pressing
Multiscale simulations
Fatigue behaviour
Structure-property relationship

ABSTRACT

Additively manufactured (AM) Ti-6Al-4V alloys face limitations in critical applications due to uncertainties in their fatigue performance. Despite extensive research on fatigue life prediction, the discrepancies in fatigue behaviour between AM structural components and material-level specimens remain poorly understood. In this study, the effect of hot isostatic pressing (HIP at 920 °C, 1000 bar Ar, 2 h) on the fatigue properties at both material and structural levels was investigated, aiming to bridge the gap in the cross-scale fatigue behaviour of AM Ti-6Al-4V alloys. Although HIP significantly improved microstructure and fatigue performance of material-level specimens, the presence of larger near-surface defects remained in the structural components, resulting in a poorer fatigue resistance. To quantitatively evaluate the impact of near-surface defects, a novel multiscale model for predicting fatigue behaviour of AM Ti-6Al-4V alloys was proposed. The model integrates finite element analysis with microstructural characteristics, where the grain boundaries (GBs) effect was quantified by the distance between GBs and the misorientations between adjacent grains. The input of this model requires only test conditions, tensile properties and microstructural information of the materials. The model was validated using *S-N* data from axial fatigue tests at both the material and structural levels, showing excellent correlation between predicted and experimental results. Overall, this study enhances the understanding of the relationship between processing techniques, microstructure and fatigue performance in AM alloys. Furthermore, it provides a multi-scale analysis framework that integrates microstructural, material and structural information, offering a basis for the accurate prediction and design of fatigue-resistant AM components.

1. Introduction

The superior comprehensive properties of titanium alloys, particularly their high-temperature performance, fatigue resistance, strength, stiffness, and corrosion resistance, have established them as ideal materials for aerospace engine blades, playing a pivotal role in the aerospace manufacturing industry [1–4]. However, their low thermal conductivity and work-hardening characteristics increase processing difficulty, classifying them as difficult-to-machine materials [5]. The inherent near-net-shape capability of additive manufacturing (AM) enhances material utilization efficiency, making titanium alloys more resource-efficient [6]. This technology demonstrates significant potential in aerospace applications, particularly for engines and space structures. Additionally, AM offers distinct advantages in fabricating complex, lightweight structures and minimizing material waste. For instance, the Airbus A350 uses Ti-6Al-4V alloy brackets manufactured with AM processes [7,8]. These brackets, designed through topology optimisation and inspired by biomimetic principles, achieve approximately 30 % weight reduction compared to traditional milling processes while maintaining structural integrity [8].

In parallel with the aerospace sector, the global railway industry is now pursuing an equally ambitious light-weighting agenda to reduce traction energy consumption and wheel-rail degradation in high-speed service. A growing body of research summarised by Zhang et al. [9] has demonstrated the feasibility of using Ti-6Al-4V for critical railway components. Notable prototype studies include TIG-welded bogie frames achieving a 38 % mass reduction while meeting both static strength and high-cycle fatigue requirements; transition couplers and primary suspension springs with a 43 % weight reduction; and investment-cast axle-box housings and additively manufactured brake

* Corresponding authors.
E-mail addresses: zhou.hongchang.jwri@osaka-u.ac.jp (H. Zhou), yanruiguo@mail.tsinghua.edu.cn (R. Yan).

https://doi.org/10.1016/j.ijfatigue.2025.109181
Received 21 May 2025; Received in revised form 15 July 2025; Accepted 18 July 2025
Available online 25 July 2025

callipers that satisfy service load demands[9]. Since unsprung assemblies such as bogie frames, suspension springs and brake systems dominate vertical dynamics, even modest mass reductions can lead to significant improvements in ride quality, infrastructure maintenance and long-term operating efficiency [9,10]. Ti-6Al-4V offers a compelling solution, being significantly lighter than conventional low-alloy steels while providing comparable yield strength. Its excellent corrosion resistance further enhances fatigue life, particularly in moisture- and salt-rich railway environments [9]. These advances underscore a pressing need for reliable multiscale fatigue data on railway grade Ti-6Al-4V, which the present work is designed to deliver.

Most fatigue specimens are currently fabricated using the laser powder bed fusion (L-PBF) technique [11–13]. Recognised as the most mature and commercially advanced AM technology, L-PBF enables the production of high-quality components with consistent properties. However, even this well-established process is not exempt from the occurrence of inherent defects associated with AM. These flaws have become a central focus of contemporary research. The layer-by-layer deposition, localised heating, and rapid cooling inherent to AM often result in microstructural defects such as lack of fusion, porosity, and unmelted particles [14–16], which significantly impair the material's mechanical performance [17,18]. Although AM titanium alloys offer many advantages, process-induced defects remain a critical limitation to their broader adoption in engineering applications [8,19]. These defects, which contribute to substantial variability in fatigue life, pose significant challenges for the reliable assessment and precise prediction of material and structure fatigue behaviour.

HIP is an effective post processing technique that uses elevated temperature and uniform gas pressure to reduce or eliminate lack of fusion defects and isolated pores generated during manufacturing, thereby increasing material density. Numerous studies have shown that HIP treatment can significantly enhance the fatigue performance of specimens [20–27]. However, some HIP treatments are frequently accompanied by microstructural coarsening [28], which consequently reduces the yield strength and ultimate tensile strength [29]. For example, Benmessaoud et al. [30] showed that an increase in grain size leads to a decrease in the critical resolved shear stress (CRSS), which promotes the early activation of slip in coarse grains and generates local heterogeneous stress concentrations, ultimately causing a reduction in the yield strength of Ti-6Al-4V. Cordero et al. reviewed six decades of Hall–Petch data on pure metals and confirmed that the Hall–Petch relationship reliably describes grain size strengthening across this broad dataset [31]. Benzing et al. demonstrated that a standard HIP cycle for Ti-6Al-4V lowers strength precisely because of microstructural coarsening [32]. Similarly, Liu et al. reported that as the α phase grain size increases, the dislocation slip length grows, dislocation pile-up is alleviated, and the macroscopic strength correspondingly decreases [33].

Although HIP significantly enhances the fatigue performance of materials-level specimens of AM Ti-6Al-4V, its effect on actual structural components is still poorly understood and has been little reported. The substantial disparity between material-level and structural-level fatigue behaviour in AM titanium alloys presents a significant challenge in engineering applications. While extensive research has been conducted on the fatigue properties of AM materials, their structural counterparts remain less explored [34–37], largely due to the substantial costs of AM and full-scale structural testing, which severely limit experimental and comprehensive research on AM structural fatigue behaviour. Furthermore, the exorbitant expenses of large-scale fatigue testing have significantly restricted comprehensive studies in this area. These financial constraints are particularly pronounced in aerospace and high-speed train systems, where rigorous validation through full-scale structural testing is essential. Consequently, selecting a robust fatigue damage model is crucial for bridging the gap between material-level assessments and structural-level fatigue predictions. Such a model would enable accurate fatigue life estimation without solely relying on costly bench testing, thereby promoting the broader adoption of AM components in practical engineering applications.

Building on this background, traction rod structures are widely used in aerospace [38,39] and rail transportation fields [40]. Within high-speed train bogies, the central traction device serves as a critical load-bearing component. Its primary functions include transmitting longitudinal traction, braking forces, and lateral constraint forces between the bogie and the car body, ensuring safe and stable operation. The design of traction rods plays a vital role in maintaining the performance of the train suspension system. This study leverages the flexibility of AM to achieve lightweight designs for traction rods and fabricate corresponding components. Through fatigue testing of these components, this study examines their differences compared to material-level fatigue behaviour and explores the specific effects of HIP on structural components.

At present, many researchers have carried out life prediction research and established related prediction models [41,42]. The visco-plastic constitutive model, which is based on the evolution of dislocation density, has garnered significant interest due to its comprehensive approach in accounting for microstructural changes like dislocation interactions and phase transformation strengthening [43,44]. These changes impact the macroscopic mechanical responses, enabling the model to effectively describe and predict material behaviour under cyclic loading conditions. It accurately captures the stress–strain response across various loading scenarios, along with the interplay between creep and fatigue interactions. Despite its capabilities, the efficacy of this model in high-cycle and very-high-cycle fatigue conditions remains to be fully validated. In such conditions, differing paths of microstructural evolution and damage accumulation could alter material responses, highlighting a need for further model development and refinement. Additionally, a life prediction method for low-cycle fatigue based on continuum damage mechanics has also gained scholarly attention [45]. Employing models of cyclic response and damage accumulation, this method has successfully simulated the low-cycle fatigue crack propagation behaviour of 316H steel at 550 °C, showing notable adaptability and accuracy. However, its treatment of stress responses in high-cycle fatigue scenarios falls short, and its applicability to aerospace materials or high-speed trains, which demand prolonged service life, is limited. The universality and extensibility of this model thus require further exploration and enhancement.

Recently, a multiscale modelling approach was introduced to predict the fatigue life and limit of ferrite-pearlite steels [46]. This model estimated total fatigue life solely based on crack growth, as supported by experimental observations. It comprised three interconnected sub-models: (i) a macroscopic finite element analysis (FEA) model, (ii) a microscopic microstructure model, and (iii) a crack growth model. The required input parameters were limited to microstructural characteristics, monotonic tensile properties, and test conditions. The predictions demonstrated strong agreement with experimental results across all tested steels. However, the applicability of this model was confined to low-grade mild steels, such as ferrite-pearlite steels, which have relatively simple microstructures characterized by grain size distributions and pearlite band thicknesses. The previous approach relied on an elliptical approximation to represent the morphology of ferrite grains and pearlite colonies. In contrast, AM titanium alloys exhibit significantly more complex geometrical features due to their hexagonal close-packed (HCP) structure. Their grain orientation and misorientation distributions differ substantially from those observed in low-grade steels, making the elliptical approximation inadequate for accurate modelling. Therefore, a more generalized method is urgently required to characterize the microstructural features associated with fatigue strength. This method must effectively address the impacts of complex microstructures on fatigue performance and ensure accurate predictions of fatigue behaviour in various materials.

Under these motivations, this research aims to develop a novel multiscale fatigue prediction model applicable to AM titanium alloys and verify the validity of the model by conducting fatigue testing and failure analysis on structural components. The key contributions of this

model are threefold: (1) it extends multiscale modelling to AM titanium alloys, addressing the complexities of their fatigue behaviour; (2) it validates the model with experimental data from structural components, bridging the gap between material-level and structural-level fatigue responses; and (3) it reveals that while HIP improves material properties, it has limited or even detrimental effects on structural components. This approach lays the groundwork for the practical application of AM titanium alloys in transport systems.

The rest of this manuscript is organised as follows: Section 2 describes the materials and methodology. Section 3 outlines the multiscale modelling approach, which consists of three sub-models. Section 4 validates the model using experimental data from structural components and explores the limitations of the HIP process in structural components. Lastly, Section 5 summarizes the key findings and conclusions.

2. Materials and methods

2.1. Mechanical properties

The AM Ti-6Al-4V coupons (i.e., the material-level specimens) and the traction rods of Ti-6Al-4V alloy were produced using the same AM process. Specifically, they were produced using a BLT-S310 3D printer employing selective laser melting (SLM) technology. The printing parameters were set as follows: laser power of 360 W, scanning speed of 1200 mm/s, scan spacing of 0.1 mm, and layer thickness of 0.06 mm. Both the AM Ti-6Al-4V coupons and four traction rods were additively manufactured, wire-cut, de-supported, polished, and subsequently heat-treated to enhance mechanical stability. To ensure alignment, the printing direction was set along the axial direction of the AM Ti-6Al-4V coupons and the longitudinal axis of the traction rods, respectively. In total, thirteen axial fatigue coupons (HIP), six tensile coupons (three HIP and three non-HIP), and four traction rods (two HIP and two non-HIP) were produced for the subsequent tests. The heat treatment involved heating the samples to 710 °C in a vacuum for 2 h, followed by cooling in an argon atmosphere. Subsequently, a subset of the AM Ti-6Al-4V coupons and two traction rods underwent HIP under controlled argon conditions at 920 °C and a pressure of 1000 bar for 2 h. For the HIP treated condition the average cooling rate is 9.7 °C min^{-1}. For the non-HIP condition, the average cooling rate is 15.6 °C min^{-1}. The chemical composition of the alloying powder (wt.%) was as follows: 5.97 % Al, 3.93 % V, 0.12 % Fe, 0.015 % C, 0.088 % O, 0.0031 % H, with the balance being Ti. All material-level coupons were polished to a gauge section roughness of $Ra = 0.20$ μm. The surface state of the traction rods was characterised with a Zygo Nexview white light interferometer. The average roughness values were $Ra = 6.19$ μm for the non-HIP rods and $Ra = 5.34$ μm for the HIP rods, respectively.

For both non-HIP and HIP-treated AM Ti-6Al-4V alloy specimens, three samples were selected for tensile testing using the Landmark servo-hydraulic testing system (MTS Systems Corporation, Eden Prairie, MN, USA). The dog-bone-shaped specimens were tested, and the resulting stress–strain curves are presented in Fig. 1(a). The elastic modulus of both non-HIP and HIP AM Ti-6Al-4V alloys was measured as 119 GPa, with a density of 4.41 g/cm^3. After HIP treatment, the tensile strength and yield strength were 946 MPa and 849 MPa, respectively. In contrast, the tensile strength and yield strength of the non-HIP specimens were 1007 MPa and 951 MPa, respectively.

The Ti-6Al-4V alloy fabricated by SLM belongs to a typical α + β titanium alloy, featuring a basketweave microstructure primarily composed of lamellar α-phase (approximately 99 %) and a small amount of β-phase (1 %). Following HIP treatment, the α-phase in the microstructure of material-level specimens becomes coarser. After HIP, the α laths coarsen appreciably: the mean grain size increases from 4.55 μm to 6.64 μm, and detailed information and schematic diagrams of the microstructure are discussed in previous work [47]. Extensive research has confirmed that HIP is highly effective in reducing or even eliminating internal defects introduced by AM processing, thereby significantly enhancing the fatigue performance of material-level specimens [25,26,28,48].

However, the effects of HIP on actual structural components remain less understood, and relevant literature is sparse. To investigate whether discrepancies exist between the AM traction rod and material AM Ti-6Al-4V coupons, Fig. 1(b) and Fig. 1(c) present the results of EBSD observations at 500 × magnification on traction rods subjected to non-HIP and HIP treatments, respectively. While HIP treatment effectively reduces internal defects at the material scale, it proves insufficient for structural applications, where defects within the structure remain challenging to eliminate.

2.2. Fatigue experiments and results

The shape and diagram of the AM Ti-6Al-4V coupon (material-level) are presented in Fig. 2(a). For structural components, the flexibility of the AM process was utilised to optimise the design of the traction rod. This optimisation was conducted based on the actual stress distribution under operational loading conditions, aiming to meet load-bearing requirements while minimising weight. The topology optimisation process was performed using the SIMP (Solid Isotropic Microstructures with Penalisation) method in OptiStruct software to achieve variable-density optimisation. For a detailed description of the topology optimisation process, refer to Section 4.1. A 3D scanner analysis showed that the surface deviation of the manufactured rods from the initial model did not exceed ± 0.5 mm, demonstrating excellent surface quality with no defects such as dents, scratches, or burrs. The shape and diagram of the traction rod are depicted in Fig. 2(b).

The material-level high frequency axial fatigue tests in this research were conducted using an MTS Landmark 200 Hz servo-hydraulic fatigue testing system, with stress ratio $R = -1$ and an actual test frequency of 120 Hz. The testing protocol adhered to the International Standard ISO 1099:2020 “Metallic materials – Fatigue testing – Axial force-controlled method.” For the traction rod structural components, two

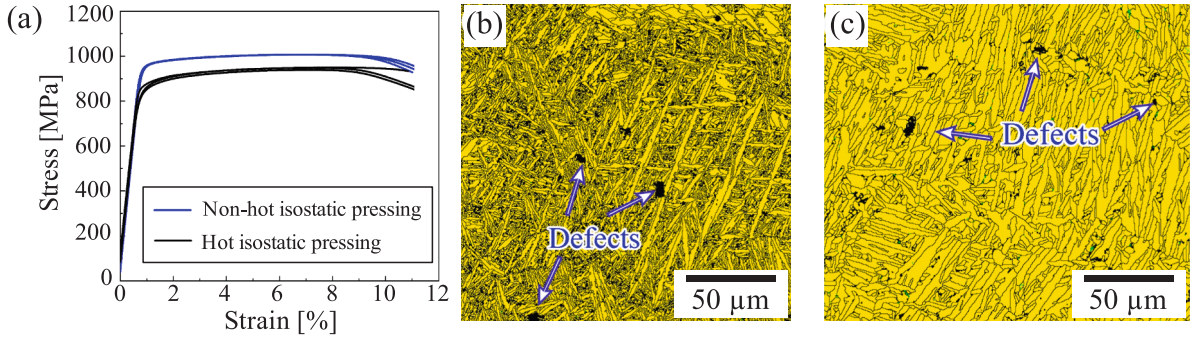

Fig. 1. (a) Stress versus strain curve of AM Ti-6Al-4V alloy. (b) and (c) are quality maps of non-HIP and HIP samples superimposed on the phase diagram, respectively.

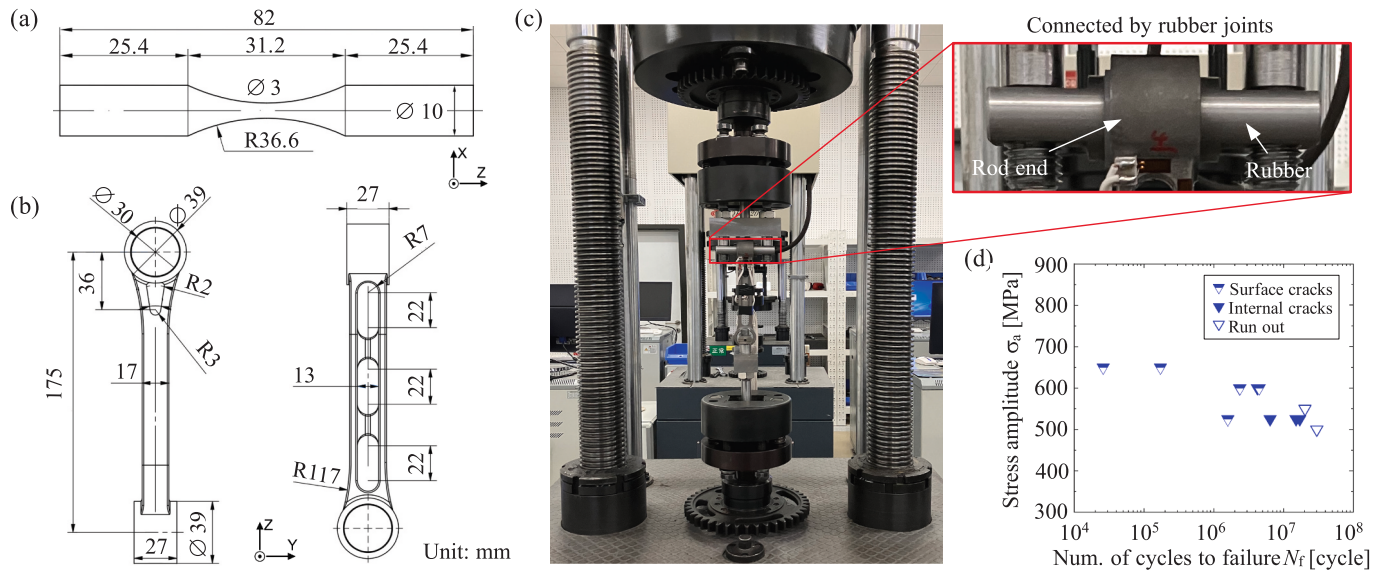

Fig. 2. (a) Diagram of the AM Ti-6Al-4V coupon for axial high-frequency fatigue testing (mm). (b) Diagram of the AM Ti-6Al-4V traction rod (mm). (c) Schematic of the axial fatigue test setup for the AM Ti-6Al-4V traction rod. (d) *S-N* data for material-level HIP Ti-6Al-4V coupon under axial loading types.

types of loading systems were employed: the QBG-100 high frequency fatigue testing machine (as shown in Fig. 2(c)), and the Shimadzu EHF-LM servo-hydraulic fatigue testing machine. The actual test frequencies during fatigue experiments were 89 Hz and 20 Hz, respectively. For the traction rod, to ensure accurate fatigue testing under a stress ratio of 0.1, a specialised fixture was specifically designed. The fixture was developed to replicate actual service conditions, ensuring that the traction rod experiences only axial loading, consistent with practical engineering applications. Additionally, the fixture configuration fully conforms to the practical engineering setup, where both ends of the traction rod are connected via rubber joints to a central pin. The tested *S-N* curve of AM Ti-6Al-4V coupon (material-level) is shown in Fig. 2(d)). It can be found that most cracks initiated from the surface, only three internal cracking cases were found near the fatigue limit.

3. Multiscale modelling strategy

This section introduces a multiscale fatigue life prediction framework to quantitatively predict fatigue performance across both material and structural scales. The detailed modelling concepts and procedures are presented in Sections 3.1 to 3.4, using a HIP Ti-6Al-4V coupon as an illustrative example, while the validity of the proposed model is demonstrated in Section 3.5. The implementation of this multiscale modelling strategy serves as an effective tool for evaluating the fatigue performance of AM Ti-6Al-4V traction rods, as discussed in Section 4.

3.1. Modelling concept

The proposed strategy is fundamentally based on estimating the total fatigue life of steels by focusing solely on crack growth life, as demonstrated in our previous experimental findings [46]. Additionally, this approach simplifies the complex three-dimensional (3D) fatigue crack growth into a two-step, two-dimensional (2D) problem. In the first step, the crack initiation site is assumed to be on the surface of structural components, aligning with the common observation that fatigue cracks typically originate at the surface (see Fig. 2(d)). In the second step, total fatigue life is assessed by modelling crack growth on an internal plane, which is assumed to be nearly perpendicular to the direction of maximum principal stress. To represent crack propagation, a semi-elliptical shape is adopted based on microtomography (Micro-CT) observations of small-crack growth in titanium alloys [49].

The proposed strategy incorporates three interconnected sub-models: (1) a macroscopic FEA model, (2) a microstructural model, and (3) a crack growth model. These sub-models were selected to capture the essential physical mechanisms across different length scales while maintaining computational efficiency and physical relevance. The required inputs, the structure of the three sub-models, and an example of the resulting output data are shown in Fig. 3. At the macroscopic level, the FEA model (Sub-model 1) is used to determine the specimen's strain field under experimental conditions, including geometry, boundary constraints, and monotonic tensile properties such as yield strength, ultimate tensile strength, and reduction in area. This approach is widely accepted and provides accurate stress–strain fields for complex geometries without excessive computational cost. At the microscopic level, the microstructural model (Sub-model 2) is implemented to account for grain-scale heterogeneities that strongly influence fatigue crack behaviour. It incorporates detailed grain characteristics, including: (i) grain major and minor axes, (ii) major axis orientation, (iii) grain orientations, (iv) Euler angles and their connectivity, and (v) grain boundary (GB) distances. Compared to homogenized crystal plasticity models, this approach offers a more direct and efficient means to quantify the role of GBs in fatigue crack evolution, particularly in capturing local microstructural barriers. The outputs from both the macroscopic FEA model and the microstructural model serve as inputs for the crack growth model (Sub-model 3), which simulates crack propagation. This model integrates macroscopic loading and microstructural effects to provide a realistic description of the crack path and rate. It was chosen over purely empirical models to ensure sensitivity to both global loading and local grain-scale resistance mechanisms.

3.2. Sub-model 1: Macroscopic finite element analysis model

Sub-model 1 aims to compute the elastic and plastic strain tensors, ε_e and ε_p, as functions of nominal stress σ_{nom} using Abaqus software, which serve as key driving factors for crack initiation and growth [50,51]. The inputs for this sub-model include experimental conditions and the monotonic tensile properties of the material under investigation. Additionally, the cyclic stress–strain (S-S) relationship is established using an empirical equation proposed by Li et al. [52], derived from the material's monotonic tensile data and expressed as:

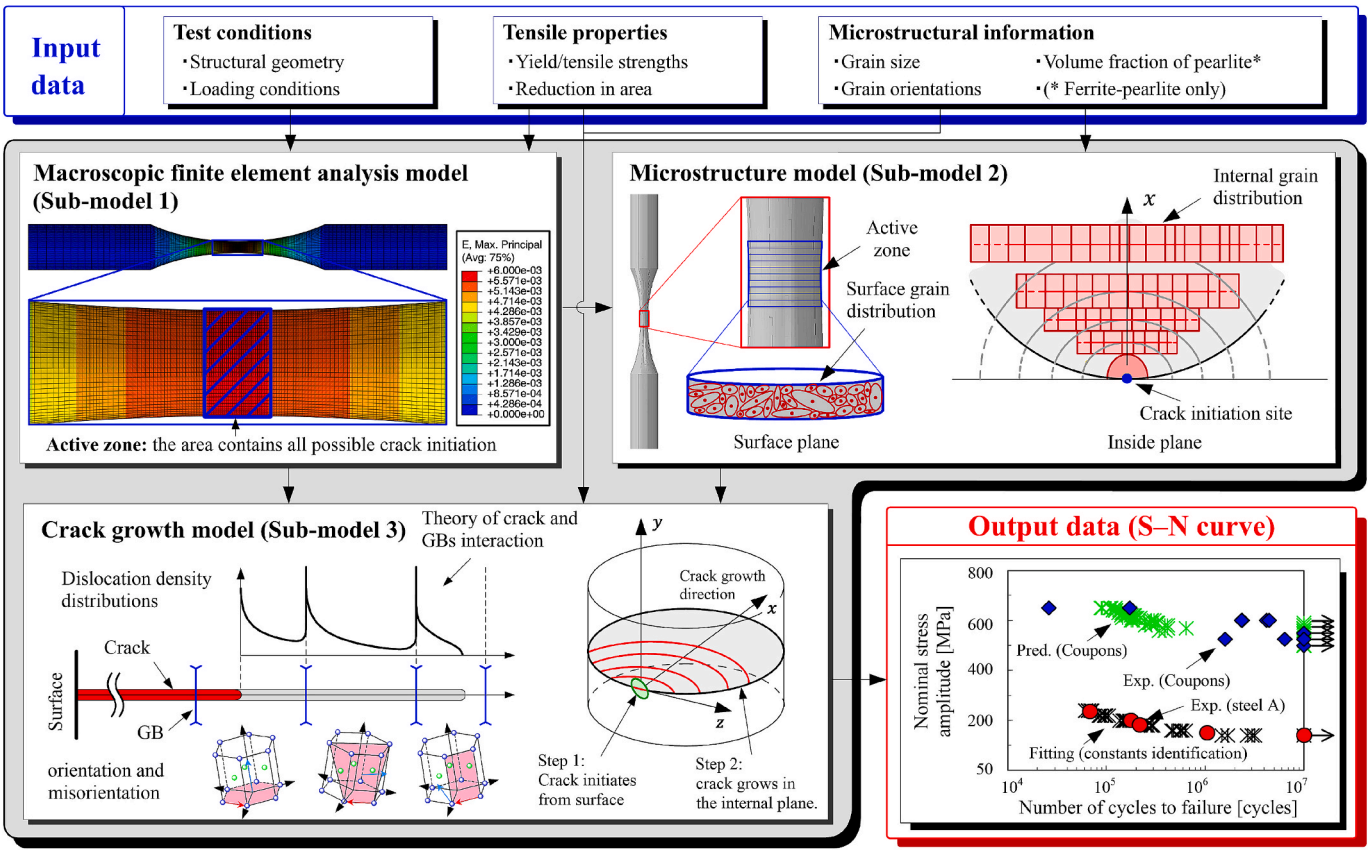

Fig. 3. Outline of the proposed multiscale modelling strategy for fatigue strength prediction.

$$\varepsilon_{eq}^{a} = \frac{\sigma_{eq}^{a}}{E} + \left(\frac{\sigma_{eq}^{a}}{K'}\right)^{\frac{1}{n'}}, \tag{1}$$

where ε_{eq}^{a} and σ_{eq}^{a} are the cyclic equivalent strain amplitude and cyclic equivalent stress amplitude, respectively; E is the Young's modulus, while K' and n' correspond to the cyclic strength coefficient and cyclic strain hardening exponent, respectively, as defined in [53].

$$K' = \begin{cases} (2.16\times10^{-4})\sigma_B{}^{2.1} + 738 & (\sigma_B/\sigma_Y \le 1.2) \\ (3.63\times10^{-4})\sigma_B{}^{2} + 0.68\sigma_B + 570 & (1.2 < \sigma_B/\sigma_Y \le 1.4) \\ 1.21\sigma_B + 555 & (1.4 < \sigma_B/\sigma_Y) \end{cases}, \tag{2}$$

$$n' = \frac{\lg K' - \lg\left(0.089(1+r_A)^{1.35}\sigma_B{}^{1.35}\left(-\frac{0.002}{\ln(1-r_A)}\right)^{0.216} + 120\right)}{\lg 500}, \tag{3}$$

where σ_Y and σ_B refer to the monotonic yield strength and ultimate tensile strength, respectively, while r_A represents the reduction of area. The parameters K' and n' in Eqs. (2) and (3) are derived from experimental data of 121 steels [53]. Utilizing these empirical equations offers a reliable approach for estimating the cyclic S-S curve. Furthermore, the cyclic yield strength σ_Y' can be determined as the 0.2 % offset yield strength based on the cyclic S-S relationship, as described in [52].

$$\sigma_Y' = K'(0.002)^{n'}. \tag{4}$$

According to Massing's hypothesis [54], the relative elastic and plastic strain tensors (ε_e and ε_p), defined as the deviations from the minimum strain values in the upper curve of the hysteresis loop, can be expressed as functions of the nominal stress σ_{nom} (i.e.,$\varepsilon_e = \varepsilon_e[\sigma_{nom}]$ and $\varepsilon_p = \varepsilon_p[\sigma_{nom}]$). These relationships are derived from FEA performed using Abaqus software considering the corresponded boundary conditions, structural geometry, and material properties of practical cases, and are formulated as follows:

$$\varepsilon_e[\sigma_{nom}] = 2\varepsilon_e'[\sigma_{nom}'], \varepsilon_p[\sigma_{nom}] = 2\varepsilon_p'[\sigma_{nom}'], \tag{5}$$

where ε_e' and ε_p' denote the elastic and plastic strain tensors corresponding to the nominal stress σ_{nom}' from the FEA results, respectively.

Although the original parameters in Eqs (2) and (3) were calibrated for steels, the functional form of the equation is widely applicable across metallic materials. Given that the present work focuses on establishing a multiscale modelling framework for AM Ti-6Al-4V alloy, rather than high-precision prediction of cyclic plasticity, this approximation provides a practical starting point. Considering the fact that most fatigue cracks typically initiate on the surface as shown in Fig. 2 (d), we defined an active zone as a surface region to contain all potential crack initiation sites, determined by the specimen geometry and loading conditions. To reduce computational costs, the active zone is restricted to regions with large-strain distributions rather than covering the entire surface. However, it remains sufficiently large to encompass surface crack initiation sites. The spatial distributions of ε_e and ε_p within this active zone are extracted from Sub-model 1, then utilised as inputs for Sub-model 3 (crack growth model), as outlined in Section 3.4. Sub-model 1 of Fig. 3 shows an example of the distribution of the maximum principal strain obtained in the macroscopic FEA of the AM Ti-6Al-4V coupon under the nominal stress amplitudeσ_a = 600 MPa and the locations of active zone.

3.3. Sub-model 2: Microstructure model

Sub-model 2 aims to generate the spatial distribution of α grains in AM Ti-6Al-4V specimens/components to assess the influence of GBs. This influence is characterized by two key factors: (i) the distances between GBs and (ii) the misorientations between adjacent grains. In this

section, the spatial arrangement of α grains is defined separately for the surface and internal planes.

3.3.1. Required data for microstructure model

The microstructure model requires data from both surface and internal planes. These data are obtained through image analysis based on measurements conducted using the electron back-scattering diffraction (EBSD) technique. Orientation Imaging Microscopy (OIM) software is employed to process EBSD measurements and perform imaging analysis [55]. A summary of the necessary microstructural information for both surface and internal planes is provided in Table 1.

The surface plane data consist of the following parameters for each grain i (i) major and minor axes (a_i, b_i), (ii) major axis angle θ_i, and (iii) grain orientations φ_i. The values for (i) and (ii) are extracted from a grain map by approximating each grain as an ellipse, as illustrated in Fig. 4(a). Meanwhile, the grain orientations φ_i are directly obtained from EBSD measurement results.

The inside plane data consist of the following key parameters:

(i) Euler angles connectivity: This represents a dataset containing the Euler angles of a target grain along with those of its neighbouring grains. These values can be directly extracted from Orientation Imaging Microscopy (OIM) software.

(ii) GBs distance t_j^i and corresponding grain width d_j^i: These values are determined through the following steps:

- Obtain the grain map from OIM (Fig. 4(b-1)) and extract grain boundary information (Fig. 4(b-2)).
- Select a grain (denoted as grain i, where $i = 1,\cdots,n_g$, with n_g being the total number of grains) from the grain map (Fig. 4(b-2)).
- Define a scanning direction (Direction-X) and create segments (Segment 1) perpendicular to Direction-X, with endpoints on the GBs. The length of each Segment 1 corresponds to the GB distance t_j^i ($j = 1,\cdots,m_i$), where m_i is the number of pixels representing grain i along Direction-X (Fig. 4(b-3)).
- Establish another scanning direction (Direction-Y), perpendicular to Direction-X. For each Segment 1, define Segments 2 with the following properties: (a) Segments 2 are perpendicular to Direction-Y, (b) their endpoints lie on GBs, and (c) they intersect with Segment 1. The average length of Segments 2 represents the corresponding grain width d_j^i (Fig. 4(b-3)).
- Repeat steps (i)–(iii) for all grains ($i = 1,\cdots,n_g$) and for all pixels along Direction-X ($j = 1,\cdots,m_i$) within each grain.

These measurements provide essential microstructural parameters for accurately modelling fatigue crack growth behaviour.

3.3.2. Microstructural modelling in the surface plane

The spatial distribution of grains on the surface plane is established within the active zone, which is determined by Sub-model 1 (Section 3.2). This active zone is discretized into surface elements, where grains are randomly assigned using the Monte Carlo method, as illustrated in Fig. 3 (Sub-model 2). Each grain is characterized by (i) major and minor axes (a_i, b_i), (ii) major axis angle θ_i, and (iii) grain orientations φ_i. The precise positioning of individual grains within each surface element is not explicitly considered. Instead, the location of each area element is assumed to be representative of all grains assigned to it. To ensure validity, the surface element size should be larger than the maximum grain size. However, using smaller area elements can improve the resolution of the crack initiation site and provide a more detailed representation of stress and strain distributions.

Table 1
Required data for the microstructure model in the surface and inside planes.

Plane	Surface	Inside
Required data	Major and minor axes (a_i, b_i) Major axis angle θ_i Euler angles φ_i	Euler angles connectivitySegment length sets (d_j^i, t_j^i) Shape change history of the crack front

3.3.3. Microstructural modelling in the inside plane

The modelling procedure for the microstructures in the inside plane consists of two steps according to the assumption of "2D problems with two steps" as shown in Fig. 5 (a). Firstly, the grain where the crack is assumed to initiate (referred to as the initial grain) is identified from the surface plane model. The shape of this initial grain in the inside plane is approximated as a semi-ellipse, aligning with the semi-elliptical crack assumption in the proposed strategy. The depth t_0 and width d_0 of the initial grain are determined based on its surface dimensions (a_i, b_i) and major axis angle θ_i, as depicted in Fig. 5 (b). For all other grains, a rectangular representation is adopted, considering the influence of GBs, as defined in Fig. 4. The length t_j^i corresponds to the GB distance along the crack growth direction, while the width d_j^i represents the effective grain width. However, the initial grain does not follow this rectangular assumption and retains its semi-elliptical shape.

The spatial distribution of grains in the inside plane is defined for each initial grain and modelled to correspond to the crack shape change history. The change in the crack shape can be calculated by the 3D fracture analysis code (FRANC3D) program [56–58]. Then, the crack aspect ratio is expressed as a function of crack depth a. The "grain line" concept, as proposed by Shibanuma et al. [46], was employed to represent all grains interacting with a potential crack front. It should be noted that the shape of the crack front is assumed to be semi-elliptical for simplification although it is an arc of a part of a semi-ellipse. An example illustrating the assignment of grains in the first grain line is provided in Fig. 5 (c) and described below.

(i) The first grain line, located next to the initial grain, is defined based on the crack front shape obtained from FRANC3D. It is characterized by an aspect ratio r_1 and a depth of $(t_0 + t_1/2)$, where t_1 denotes the average thickness of the first grain line (Fig. 5(c-1)).

(ii) The 1st grain with the width d_1^1 and length t_1^1 is assigned to the first grain line, which is transformed into an equivalent straight line of the same length (Fig. 5(c-1)).

(iii) The 2nd grain with the width d_2^1 and length t_2^1 is assigned next to the 1st grain (Fig. 5(c-2)).

(iv) Repeat to assign the i-th grain next to the (i-1)-th grain until the sum of all assigned grains' width equals the grain line length l_1, i.e., $\sum_{j=1}^{n_1} d_j^1$, where n_1 presents the number of grains in the 1st grain line(Fig. 5(c-3)).

The procedure for assigning grains in the i-th grain line (i = 2, 3, …) follows the same method as that used for the 1st grain line. The thickness of the i-th grain line t_i is defined as the average value of the length of all the grains, i.e., $t_i = \frac{1}{n_1}\sum_{j=1}^{n_1} t_j^1$ (Fig. 5(d-1)). The grain assignment continues until the cumulative sum of t_i equals the specimen thickness t, i.e., $\sum_{i=1}^{n} t_i \rightarrow t$. Subsequently, the location of each effective GB is determined as the boundaries of each grain line as $L_i = \sum_{j=0}^{i-1} t_j$ (i =1, 2, …) (Fig. 5(d-2)).

After assigning the grain geometry, each grain line is normalized relative to its length l_i. Subsequently, the grain orientations are determined. The orientation of the initial grain is directly obtained from the Euler angle data on the surface plane, while the orientations of subsequent grains are assigned based on Euler angle connectivity. Only connectivity along the crack growth direction (i.e., thickness direction) is considered, as misorientations in the circumferential direction have minimal impact on crack growth (Fig. 5(d-3)) [59].

The spatial distribution of grains in the inside plane, established

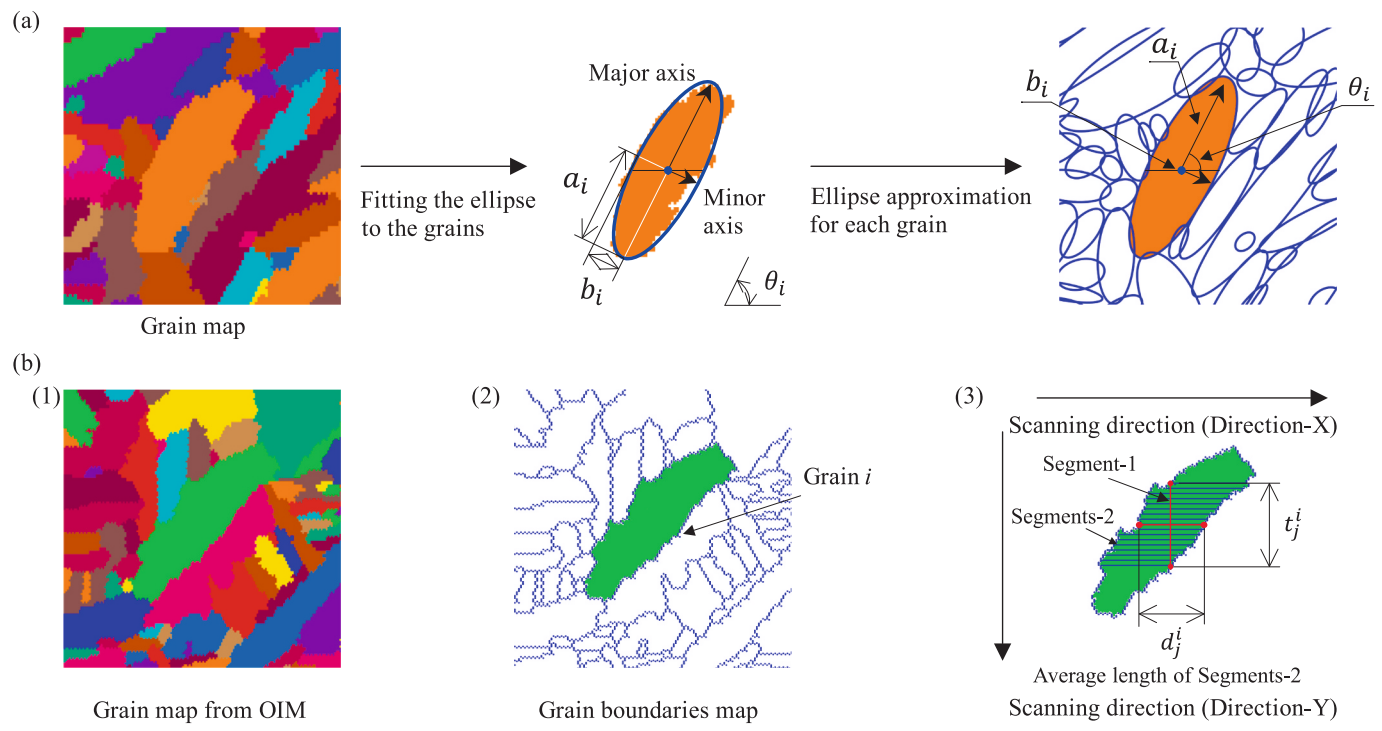

Fig. 4. (a) The image analysis process uses an ellipse approximation to represent grains on the surface plane. (b) Measurement of GB distances (1) grain map from OIM, (2) extract grain boundary information, and (3) definition of Segment 1 with length t_j^i and Segments 2 with average length d_j^i.

through this process, serves as the computational unit for Sub-model 3, which is discussed in Section 3.4.

3.4. Sub-model 3: Crack growth model

This section introduces an integrated crack-growth law to calculate the fatigue crack growth rate (da/dN) first. Thereafter, the detailed procedures for assessing fatigue life are described.

3.4.1. Integrated crack-growth law

The crack growth rate (da/dN) is calculated using an integrated crack-growth law considering micro/macro crack growth behaviour in three regimes, as shown in Fig. 6(a) and Eq. (6). In regimes I and II, fatigue crack growth is dominant by microstructures so that the crack/GBs interaction theory proposed by Tanaka et al. [60] based on the continuously distributed dislocation theory [61] is employed. This theory enables the evaluation of da/dN as a function of the crack-tip sliding displacement range, $\Delta CTSD$, and material constants C, n, and $\Delta CTSD_{\mathrm{th}}$. It should be noted that the boundary of regime I (L_1) is determined by the first grain boundary, indicating that regime I is accounted for the crack growth in the first grain. The boundary of regime II (a_2) is set as 2 mm, which has been proved to be effective in our previous study [50,62]. In regime III, fatigue cracks are sufficient long, and the influence of microstructures becomes negligible. Therefore, da/dN is calculated by the Paris' law, which is widely adopted for macro-crack problems with high efficiency [63].

$$\frac{da}{dN}=\begin{cases} C\bullet\Delta CTSD^{n} & (\text{in regime I}\,(0\le a\le L_1)) \\ C\bullet(\Delta CTSD^{n}-\Delta CTSD_{\mathrm{th}}{}^{n}) & (\text{in regime II}\,(L_1<a<a_2)) \\ C^{'}\bullet\Delta K_{\mathrm{eff}}^{m} & (\text{in regime III}\,(a_2<a)) \end{cases}. \tag{6}$$

The constants C and n are intrinsic material properties, remaining consistent across all types of polycrystalline metals and not subject to adjustment for individual cases. In regime II, da/dN incorporates the threshold parameter $\Delta CTSD_{\mathrm{th}}$, which reflects the influence of multiple slip systems activation [64]. The constants in Paris' law, C' and m, in regime III are determined based on the da/dN curve generated in regime II, as shown in the range of (a_1, a_2) in Fig. 6(a), where $a_1 = 1$mm. The number of cycles N is determined by integrating the inverse of Eq. (6) with respect to a specified crack depth a.

In Eq. (6), $\Delta CTSD$ is applicable to any crack modes, as it can be calculated under arbitrary stress tensors, as proved in our previous study [21,24], expressed as:

$$\Delta\mathrm{CTSD}=\frac{4(1-\nu)}{\pi G}\left[2a\tau_j^{\mathrm{f}}\ln\left(\frac{c}{a}\right)+\Delta\tau_j\sum_{i=j+1}^{\infty}\left(\frac{\tau_i^{\mathrm{f}}}{\Delta\tau_i}-\frac{\tau_{i-1}^{\mathrm{f}}}{\Delta\tau_{i-1}}\right)g[a,c,L_{i-1}]\right],$$

$$g[a,c,L]=L\ln\left|\frac{\sqrt{c^2-L^2}+\sqrt{c^2-a^2}}{\sqrt{c^2-L^2}-\sqrt{c^2-a^2}}\right|-a\ln\left|\frac{a\sqrt{c^2-L^2}+L\sqrt{c^2-a^2}}{a\sqrt{c^2-L^2}-L\sqrt{c^2-a^2}}\right|,$$

$$\frac{\pi}{4}-\frac{\tau_j^{\mathrm{f}}}{\Delta\tau_j}\arccos\left(\frac{a}{c}\right)-\sum_{i=j+1}^{\infty}\left(\frac{\tau_i^{\mathrm{f}}}{\Delta\tau_i}-\frac{\tau_{i-1}^{\mathrm{f}}}{\Delta\tau_{i-1}}\right)\arccos\left(\frac{L_{i-1}}{c}\right)=0, \tag{7}$$

where G and ν represent the shear modulus and Poisson's ratio, respectively. The variable j represents the sequence of the grain line at the location of the crack tip. The parameters a and c denote the crack depth and slip band length, respectively. L_i ($i = 1, 2, \cdots$) indicates the positions of effective GBs, as illustrated in Fig. 5(d-2). A schematic illustrating the relationship between a, c, and L_i is presented in Fig. 6(b).

In Eq. (7), τ_i^{f} denotes the frictional strength for dislocation movement and is derived from the Hall-Petch law [65] as:

$$\tau^{\mathrm{f}}=\frac{\sigma_{\mathrm{Y}}{}'}{\sigma_{\mathrm{Y}}}\tau^{\mathrm{f(s)}},$$

$$\tau^{\mathrm{f(s)}}=\frac{1}{2}(\sigma_{\mathrm{Y}}-\frac{k}{\sqrt{d}}), \tag{8}$$

where $\sigma_{\mathrm{Y}}{}'$ represents the cyclic yield strength, which is determined as the 0.2 % offset yield strength from the cyclic S–S relationship in Eq. (1). $\tau^{\mathrm{f(s)}}$ denotes the shear strength of a single crystal under monotonic loading. k

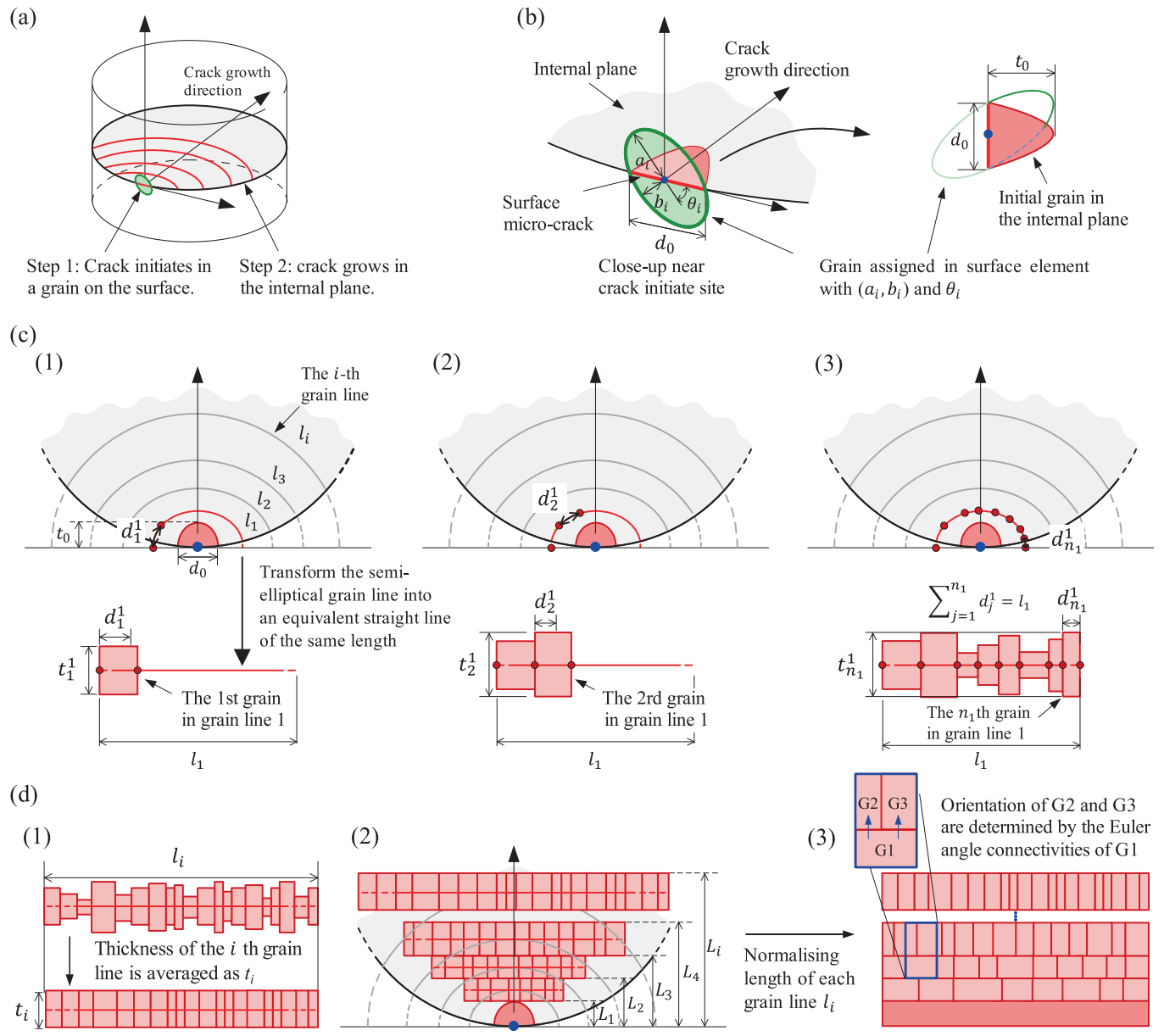

Fig. 5. Spatial distribution of grains in the inside plane. (a) fatigue crack growth as "2D problems with two steps" (b) define initial grain shape (t_0 and d_0 are the depth and width of the initial grain shape, respectively), (c) an example of assigning grains to the grain line, and (d) assignment of grain orientations.

is the Hall–Petch coefficient, which is assumed to be 23.4 MPa$\sqrt{\text{mm}}$ for mild steel [66], and 13.2 MPa$\sqrt{\text{mm}}$ for Ti-6Al-AV corresponding to the grain size ranging between 0.6 and 7.5 μm [30]. $\bar{d}$ represents the average grain size, defined in terms of GB obtained from Section 3.3.1.

$\Delta\tau_i$ in Eq. (7) denotes the range of effective resolved shear stress in the i-th grain. This parameter accounts for the reduction in slip dislocation density near the crack tip due to misorientations between adjacent grains and is expressed as follows [67]:

$$\Delta\tau_i = \max_{k=1\cdots5}[(\mathbf{n}_k)_i^{\mathrm{T}} \bullet \Delta\sigma_{i-1} \bullet (\mathbf{m}_k)_i], \tag{9}$$

where $(\mathbf{n}_k)_i$ and $(\mathbf{m}_k)_i$ represent the unit normal vector of the k-th ($k = 1, 2, \cdots, 5$) slip plane and slip direction in the i-th grain, respectively, as illustrated in Fig. 6(c). $\Delta\sigma_{i-1}$ is the effective stress range tensor for the $(i-1)$-th grain, which is expressed as:

$$\Delta\sigma_{i-1} = \begin{cases} \Delta\sigma_{\mathrm{eff}}[a] & (i=j) \\ \Delta\tau_{i-1}(\mathbf{n}_k)_{i-1}^{T} \times (\mathbf{m}_k)_{i-1} & (i \geq j+1) \end{cases}, \tag{10}$$

where $\Delta\sigma_{\mathrm{eff}}$ is the effective stress range tensor at crack depth a, incorporating the influence of crack opening and closure behaviour, given by:

$$\Delta\sigma_{\mathrm{eff}}[a] = \sigma_{\mathrm{eff}}[\sigma_{\max}, a] - \sigma_{\mathrm{eff}}[\sigma_{\mathrm{op}}, a], \tag{11}$$

where $\sigma_{\max}$ and σ_{op} denote the maximum nominal stress and crack opening stress, respectively. The equations used to derive σ_{eff}, $\sigma_{\max}$, and σ_{op} are provided in detail in Appendix A.

ΔK_{eff} represents the range of effective stress intensity factor (SIF), accounting for the influence of crack opening and closure behaviour, and is expressed as:

$$\Delta K_{\mathrm{eff}}[\sigma_{\mathrm{nom}}, a] = K[\sigma_{\max}, a] - K[\sigma_{\mathrm{op}}, a]. \tag{12}$$

The calculation of K is provided in Eq. (A.3) in Appendix A.

3.4.2. Evaluation of fatigue life

The fatigue life N_{f} is determined by analysing crack growth through the following systematic procedure.

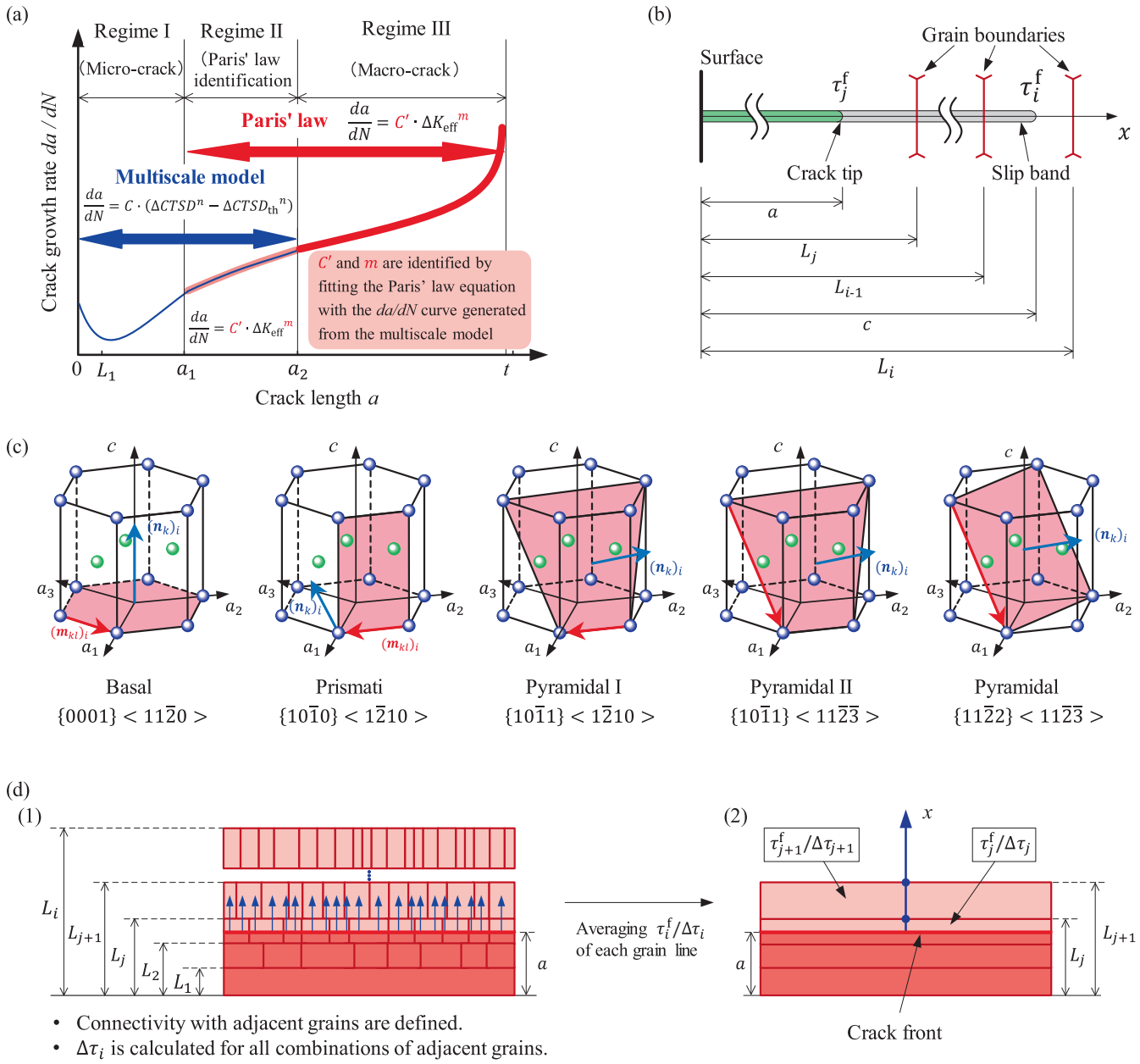

Fig. 6. (a) The integrated crack-growth law in three regimes. (b) Relationship between a, c, and L_i ($i = 1,2,\cdots$) in the crack and GB interaction theory [60]. (c) Active slip system in α-phase Ti-6Al-4V alloy. (d) Evaluating the average $\tau_i^{\mathrm{f}}/\Delta\tau_i$ in each grain line. (1) calculate $\Delta\tau_i$ for each grain considering the grain misorientation, and (2) average $\tau_i^{\mathrm{f}}/\Delta\tau_i$ for each grain line.

(i) *Crack Initiation Assumption*: Fatigue cracks are assumed to initiate at individual grains within the surface elements of the active zone.

(ii) *Defining Crack Depth Range*: A range of crack depths is specified as $a \in [0, a_2]$ ensuring sufficiently fine intervals to achieve high solution accuracy.

(iii) *Calculation of* $\Delta\tau_i$: For each grain, the effective resolved shear stress range $\Delta\tau_i$ is computed, considering grain misorientation as modelled in Fig. 5(d-3) using Eq. (9) (an shown in Fig. 6(d-1)).

(iv) *Evaluation of Shear Strength Ratio*: The ratio $(\tau_i^{\mathrm{f}}/\Delta\tau_i)$ is determined for each grain within the i-th normalised grain line ($i = j, j+1, \cdots$). The average $\tau_i^{\mathrm{f}}/\Delta\tau_i$ for the i-th grain line is then used in Eq. (7) (an shown in Fig. 6(d-2)).

(v) *Sequential Crack Growth Analysis*: The slip band length c, the crack-tip sliding displacement range $\Delta CTSD$, and the crack growth rate da/dN are sequentially computed for each crack depth a using Eqs. (6) and (7).

(vi) *Identification of Paris' Law Constants*: The Paris' law constants C' and m are identified by fitting the crack growth law in regime III to the da/dN curve derived from regime II (Fig. 6(a)). These constants are then used to evaluate da/dN in regime III over the range (a_2, t).

(vii) *Fatigue Life Calculation*: The inverse of da/dN is integrated as a function of a until $a = t$ to determine the number of cycles to failure for all crack initiation sites.

(viii) *Final Fatigue Life Determination*: The fatigue life of the specimen N_{f} is identified as the minimum number of cycles to failure among all crack initiation sites.

3.5. Strategy validation

In this section, the proposed multiscale modelling strategy is validated by comparing the predicted fatigue lives from material-level fatigue tests with corresponding experimental results.

The mechanical and microstructural properties of AM Ti-6Al-4V, derived from tensile tests and Eq. (8), are summarized in Table 2. σ_Y, σ_B, and r_A are used in the material model for Abaqus simulation introduced in FEA model.

To implement the integrated crack-growth law introduced in Section 3.4.1, the material constants C, n, and $\Delta CTSD_{th}$ should be determined first. Although these parameters have only been validated for ferrite-pearlite steels in previous work [50,51,62,68], this study assumes their applicability to all polycrystalline metals, including the Ti-6Al-4V alloy. Therefore, we identify C, n, and $\Delta CTSD_{th}$ by fitting the simulated S-N curve of one ferrite-pearlite steel (Steel A) to its corresponding experimental data from the literature [68]. The resulting values are $C = 15.5$, $n = 1.8$, and $\Delta CTSD_{th} = 1.12 \times 10^{-4}$ mm. Comprehensive details on Steel A, including test conditions, results, and the parameter identification process, are provided in Appendix B.

The S–N data of material-level AM Ti-6Al-4V coupons (with six values computed for each load level) were predicted using the identified integrated crack-growth law in the multiscale model. Fig. 7 compares the predicted S–N curves with experimental results, showing a strong correlation, particularly in terms of the fatigue limit. These findings highlight the significant influence of microstructural characteristics on high-cycle fatigue life. Notably, data dispersion is more pronounced at lower load amplitudes and gradually decreases as the load amplitude increases. The results confirm that the proposed multiscale fatigue model is not only applicable to conventional mild steel but also extends to AM titanium alloys. In other words, this approach has the potential to serve as a general framework for fatigue analysis in various polycrystalline metals. The required input data for the model are minimal, including only: (i) microstructural information, (ii) monotonic tensile properties of materials, and (iii) test conditions.

4. Application of multiscale fatigue model to structural scale

Despite extensive research on the load bearing capacity and fatigue performance of AM material-level specimens, particularly the effects of defects, researchers focusing on the load-bearing capacity and fatigue behaviour of AM structural components are relatively scarce [38,39]. Extensive research, including our previous work, has demonstrated that HIP treatment effectively reduces internal defects and significantly enhances the fatigue performance of AM Ti-6Al-4V alloy material-level specimens. However, as shown in Fig. 1, HIP treatment has limited efficacy in eliminating defects within structural components, and relevant literature on this issue remains scarce. Therefore, this study aims to perform fatigue testing and failure analysis on structural components, compare their behaviour with material-level fatigue performance, and investigate the specific impacts of HIP treatment on structural components. Consequently, the multiscale fatigue model developed for AM material-level specimens is applied to the structural components considering the effect of defects. These findings provide experimental foundations and theoretical guidance for the practical application of AM titanium alloys in transport systems.

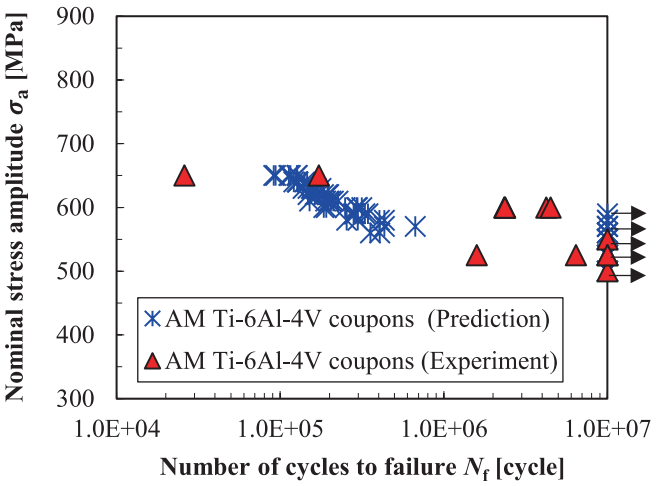

Fig. 7. Predicted results of S–N curves compared with experimental results of AM Ti-6Al-4V coupons.

4.1. Topology optimisation of traction rod structure

In high-speed train bogies, the bogie frame, as the most critical load-bearing structure between the car body and the wheels, plays an essential role in traction, braking, and stable operation. According to EN 13749 [69] newly commissioned bogie frames must undergo simulations and tests to verify their structural strength. As a key load-transmitting structure within the central traction device, traction rods are primarily used in conjunction with rubber joints. The rubber joint is press-fitted into the traction rod with an interference fit, enabling connections between the traction beam and the bogie frame. Under exceptional conditions, the longitudinal impact load on the central pin is calculated based on a train acceleration of 3g as follows:

$$F_{xD} = 3g \times (m^{+} - m), \tag{13}$$

where m^{+} is the mass of the train bogie, including the bolster and central pin (8885 kg), and m is the mass of the central pin and traction beam connection (558 kg). For a single traction rod, the longitudinal impact load is calculated as $F_{xD1} = F_{xD2} = F_{xD}/2$, yielding a value of 122.6 kN.

Under normal braking conditions, according to EN 13749 [69], the longitudinal load on the bogie is given by:

$$F_x = 1.1 \times a_N \times 2P, \tag{14}$$

where a_N is the normal braking deceleration (1.1 m/s^2), and **P** is the axle load (15 t). For a single traction rod, the longitudinal braking load is calculated as $F_{x1} = F_{x2} = F_x/2$, yielding a value of 18.2 kN.

For traction rods in long-term operation under complex fatigue conditions, direct testing provides an ideal, accurate method for determining structural load characteristics. This approach enables detailed recording of load histories under various conditions, including train startup traction, high- and low-speed operation, gradient negotiation, and braking. These data not only elucidate the performance of traction rods under normal operating conditions but also reveal their load response characteristics under exceptional circumstances.

To comprehensively explore the variations in load characteristics of

Table 2
Mechanical and microstructural properties of AM Ti-6Al-4V.

Steel	Monotonic yield strength σ_Y [MPa]	Cyclic yield strength σ_Y' [MPa]	Tensile strength σ_B [MPa]	Reduction in area r_A [-]	Average grain size $\bar{d}$[μm]	Friction strength to move dislocations τ^f [MPa]
AM Ti-6Al-4V	849	745	946	0.39	4.9	290.7

high-speed train traction rods across different operational stages, this study conducted detailed statistical analyses of the full experimental dataset, leading to the development of a load spectrum for the traction rod, as shown in Fig. 8(a). The spectrum reveals that during high-speed operation, the maximum load amplitude reaches 35.44 kN, which is significantly lower than the impact load under exceptional conditions. Furthermore, as the dynamic load amplitude decreases, its frequency of occurrence increases, indicating that traction rods primarily endure frequent low-amplitude loads during regular operation.

According to Miner's rule for cumulative fatigue damage, the main factors contributing to structural fatigue damage are load amplitude and frequency. The relative fatigue damage for each load level is calculated using the following equation:

$$d_i = \frac{D_i}{D} = \frac{F_i^m N_i}{\sum_{i=1}^{n} F_i^m N_i}, \tag{15}$$

where D_i represents the fatigue damage caused by the i-th load level F_i acting for N_i, while D is the total cumulative damage contributed by all load levels. The material constant m, set at 26.76, is derived from the median S-N curve data of material-level specimens under axial high-frequency loading for HIP-treated Ti-6Al-4V alloy.

Based on this equation, the damage ratio d_i relative to 15 million kilometres of service can be calculated and compared with actual fatigue test results, verifying whether the designed traction rod meets fatigue-resistant design standards.

To meet the lightweight requirements of high-speed trains, the flexibility of AM was leveraged to optimize the design of the traction rod structure. This design aimed to achieve the lightest possible weight while satisfying load-bearing requirements based on stress distribution under actual loading conditions. The solid isotropic microstructures with penalization principle were employed using OptiStruct software for variable density topology optimisation. Initially, a simulation under exceptional load conditions was performed on the original traction rod structure, with the stress distribution shown in Fig. 8(b-1). Under these conditions, the maximum stress was concentrated at the circular arc at the rod end, reaching 162.7 MPa.

The optimisation design accounted for the worst-case longitudinal impact load, setting F_z to 122.6 kN. A mass fraction constraint was imposed with an upper limit of 0.2, while a stress constraint ensured that the maximum allowable stress remained below 849 MPa, corresponding to the yield stress of Ti-6Al-4V. The optimisation objective was to maximize stiffness, with the convergence criterion defined as regular convergence. Specifically, this required the target tolerance to fall below 0.003 after two consecutive iterations, while staying within 1 % of the constraint limits. The inner wall of the traction rod sleeve was designated as a non-design region to facilitate installation and load transfer, as highlighted in red in Fig. 8(b-2), while the blue areas represent the topology-optimized regions. With one end of the traction rod fully constrained in the negative z-axis direction and a tensile load of 122.6 kN applied along the positive z-axis, the OptiStruct software achieved convergence after 35 iterations, meeting all constraints. The resulting topology optimisation is illustrated in Fig. 8(b-3).

Considering equipment limitations and cost, a 3:1 scaled-down traction rod was printed for testing. The geometric shape derived from the optimisation results was redesigned and subjected to finite element stress analysis. After multiple iterative analyses, the final dimensions of the optimized traction rod are shown in Fig. 2(b), with the printed physical model depicted in Fig. 2(c). The volume of the original traction rod model was 2357.26 cm, while the optimized model volume was reduced to 1395.57 cm, approximately 59.20 % of the original. Coupled with the low density of titanium alloys, the optimized traction rod's weight was reduced by 66.74 %, achieving the goal of lightweight design.

4.2. Fatigue performance of AM Ti-6Al-4V traction rod

Dimensional analysis indicates that reducing the structural size by a factor of three necessitates a ninefold reduction in load to maintain equivalent stress levels. Consequently, the theoretical maximum longitudinal impact load for the scaled-down traction rod was calculated to be 16.04 kN. Incorporating a fatigue safety factor of 1.4, the maximum design experimental load was set at 22.39 kN, with a stress ratio 0.1 and a frequency range of 20–89 Hz. Prior to conducting fatigue tests, the stress distribution of the optimised traction rod under exceptional loading conditions was analysed using Abaqus. During the static analysis, an axial concentrated force of 22.39 kN was applied to half of the bolt hole at one end of the rod along the z-axis, while the bolt hole on the opposite side was fully constrained. The mesh consisted of hexahedral elements (C3D8R) with a size range of 0.3–0.5 mm.

The maximum principal stress distribution is shown in Fig. 9. Finite element analysis revealed that the maximum stress, 572.1 MPa, occurred at the inner arc of the sleeve wall (position 1 in Fig. 9(a)). Aside from this region, the highest stress on the central linkage of the traction rod was located at position 2 with a calculated value of 563.4 MPa. During fatigue testing, strain gauges were used to measure stress at critical locations, with measured stress values for the four rods showing an error of less than 7 %. The average maximum stress amplitude measured at the same location across all four rods was 553.6 MPa (indicated in blue in Fig. 9(a), with a deviation of less than 1.77 % from the simulated results.

The measured stress amplitudes at position 2 were plotted alongside the material-level S-N data for axial fatigue loading in Fig. 9(c). Comparative analysis revealed that the fatigue performance of the AM Ti-6Al-4V traction rods exhibited no significant degradation compared to the material-level specimens. However, the HIP post-processing did not result in a noticeable improvement in the fatigue performance of

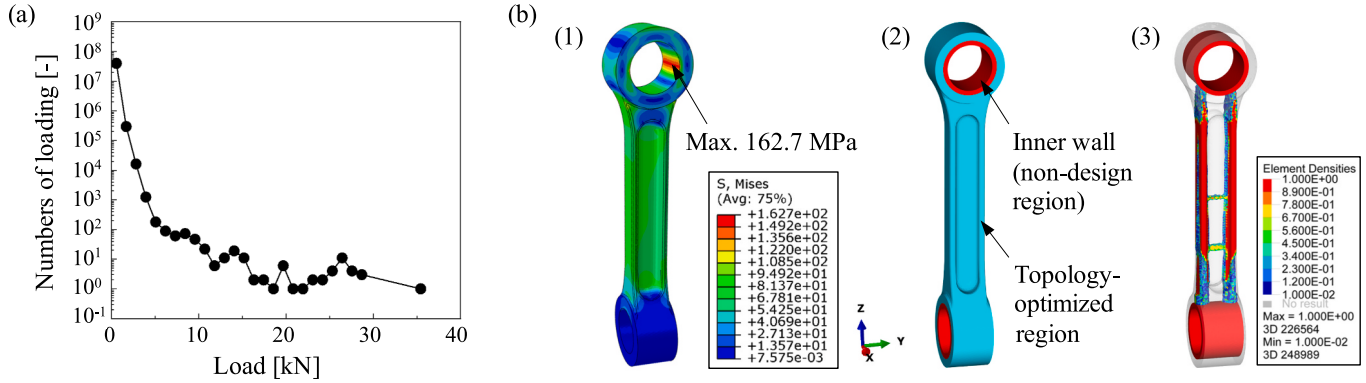

Fig. 8. (a)Measured load spectrum of traction rod (2400 km). (b): (1) Von Mises stress map under exceptional load conditions for the traction rod. (2) Schematic of the topology optimisation area for the traction rod. (3) Topology optimisation results.

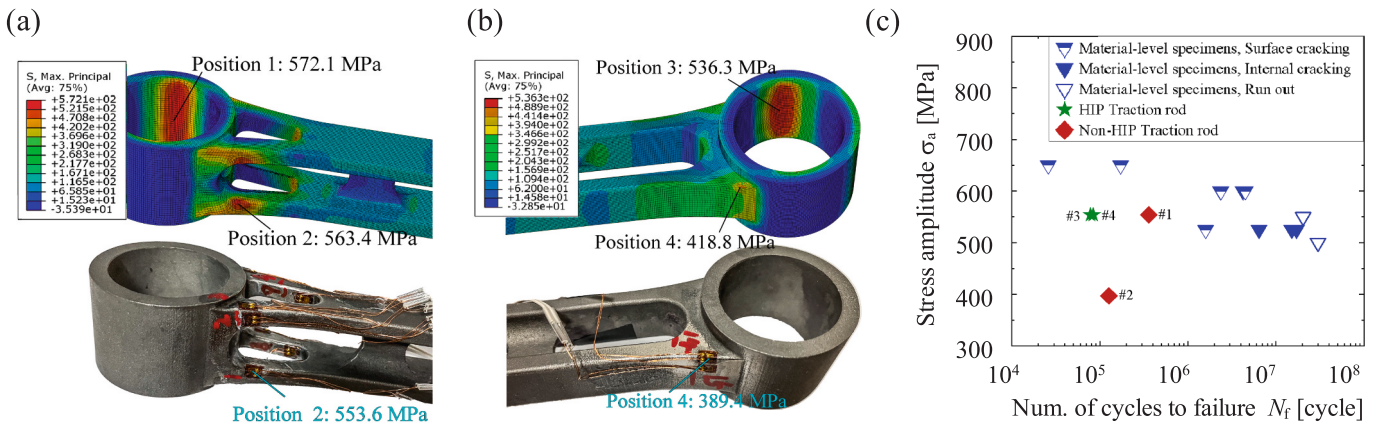

Fig. 9. (a) and (b) Maximum principal stress contour map at both ends of the traction rod under a 22.39 kN load along the z-axis. (c) Comparison of axial fatigue load *S-N* data of AM Ti-6Al-4V alloy specimens and *S-N* data from tensile rod fatigue tests.

structural components compared to material-level behaviour.

4.3. Microstructural observations

Fig. 10 (a) depicts the fracture location of the non-HIP traction rod No. 1. The crack initiation site as a single point is located on the inner wall surface of the sleeve, as shown in Fig. 10 (b). To further investigate the differences in fatigue behaviour between traction rods and material-level specimens, SEM was performed on the fracture surfaces of the rods. The crack grows outward through the sleeve, leading to final fracture. The fatigue crack initiation and growth regions are delineated in Fig. 10 (c) with dashed lines. Detailed SEM examination revealed that the fatigue crack initiated at an unmelted defect near the sleeve's inner wall surface, as shown in Fig. 10(c-1) ~ (c-3). Unmelted powder particles were observed within the defect, as well as a larger unmelted defect beneath the crack initiation site.

Considering the diversity of defect morphologies, appropriate parameters must be established to evaluate their influence. Typically, in irregularly shaped defects, fatigue cracks tend to initiate at the deepest concave corners, where the stress intensity factor is highest. When defects exhibit morphologies similar to those shown in Fig. 10(c-2), their effective size, $\sqrt{area_{eff}}$, rather than their actual dimensions, must be considered [70–73]. In Fig. 10(c-3), the yellow solid line indicates the actual contour of the defect, while the green solid line represents the smoothed contour surrounding the irregular defect shape, used for estimating the effective defect area.

The fatigue fracture location of the Non-HIP No.2 traction rod was also found at the inner wall of the sleeve end, as shown in Fig. 11. Its fatigue cracks exhibited multiple initiation sites, with two prominent crack origins identified (Fig. 11(b)). Crack initiation site 1 was associated with two adjacent lack-of-fusion defects, as depicted in Fig. 11(c-1). In such cases, the interaction between adjacent defects must be considered [70–73]. Typically, fatigue cracks initiated from a single defect may coalesce with adjacent defects, resulting in an effective

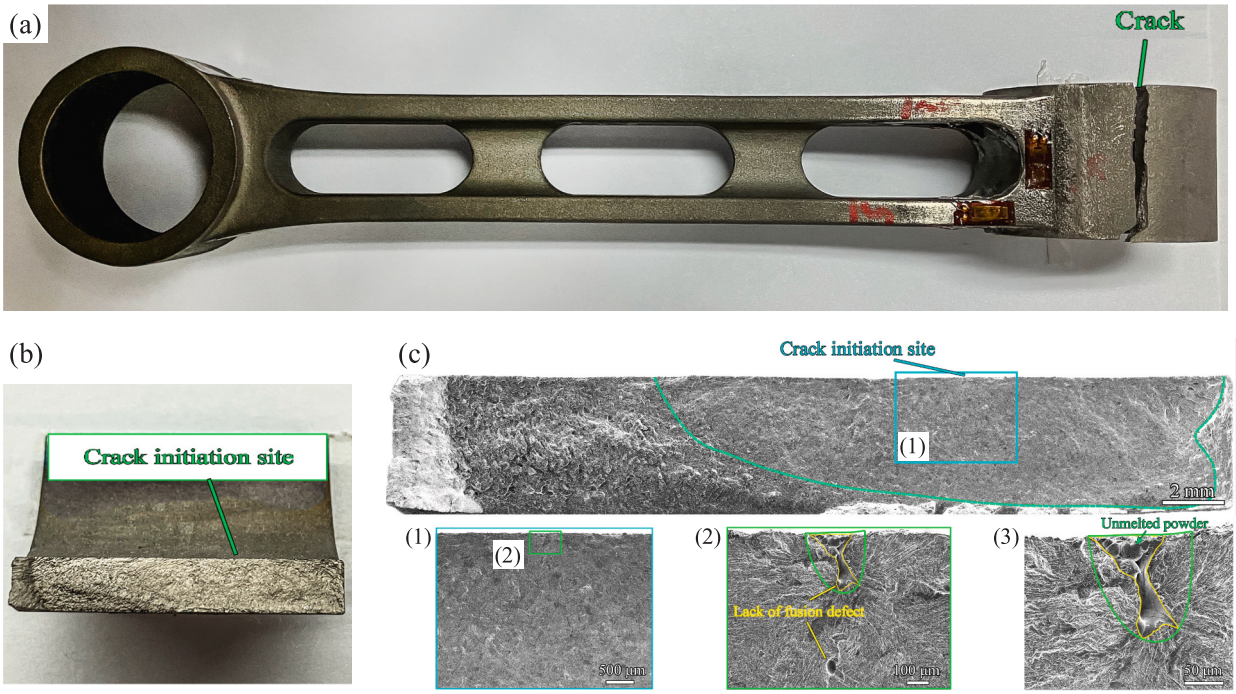

Fig. 10. (a) Physical photo of fracture location of non-HIP traction rod No.1 at 22.39 kN, 3.59 × 10^5 cycles; (b) is the enlarged image of the fracture location in (a). (c) SEM observation: (1) Magnified view of the rectangular framed area in (c); (2) Magnified view of the rectangular framed area in (1); (3) Enlarged view of the defect at the crack initiation site.

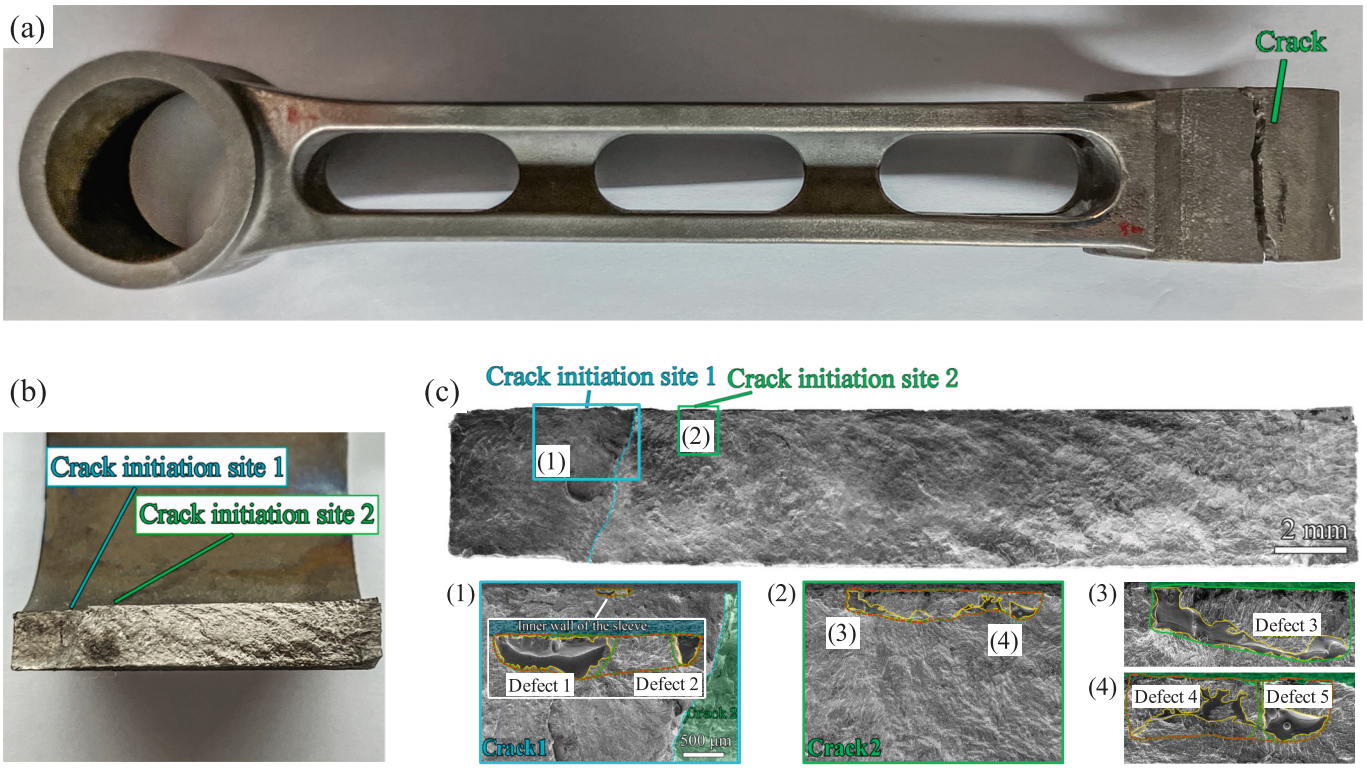

Fig. 11. (a) Physical photo of fracture location of non-HIP traction rod No.2 traction rod under 16.04 kN, 1.27 × 10^5 cycles. (b) is the enlarged image of the fracture location in (a). (c) SEM observation: (1) Magnified view of defects 1 and 2. (2) Crack initiation site 2. (3) Magnified view of defect 3. (4) Magnified view of defects 4 and 5.

defect size significantly larger than that of individual defects. Surface defects are generally more detrimental than subsurface or internal defects [70]. The effective defect size of two closely spaced defects was estimated using a smoothed contour line encompassing both defects, as shown by the red dashed line. Similarly, crack initiation site 2 involved three adjacent lack-of-fusion defects, as shown in Fig. 11(c-2). The effective size of these defects was estimated using a smoothed contour line surrounding all three defects. The effective defect sizes for Defects 1 through 5 are represented by green lines. The red dashed line in Fig. 11 (c-4) provides the effective defect size for the interaction of Defects 4

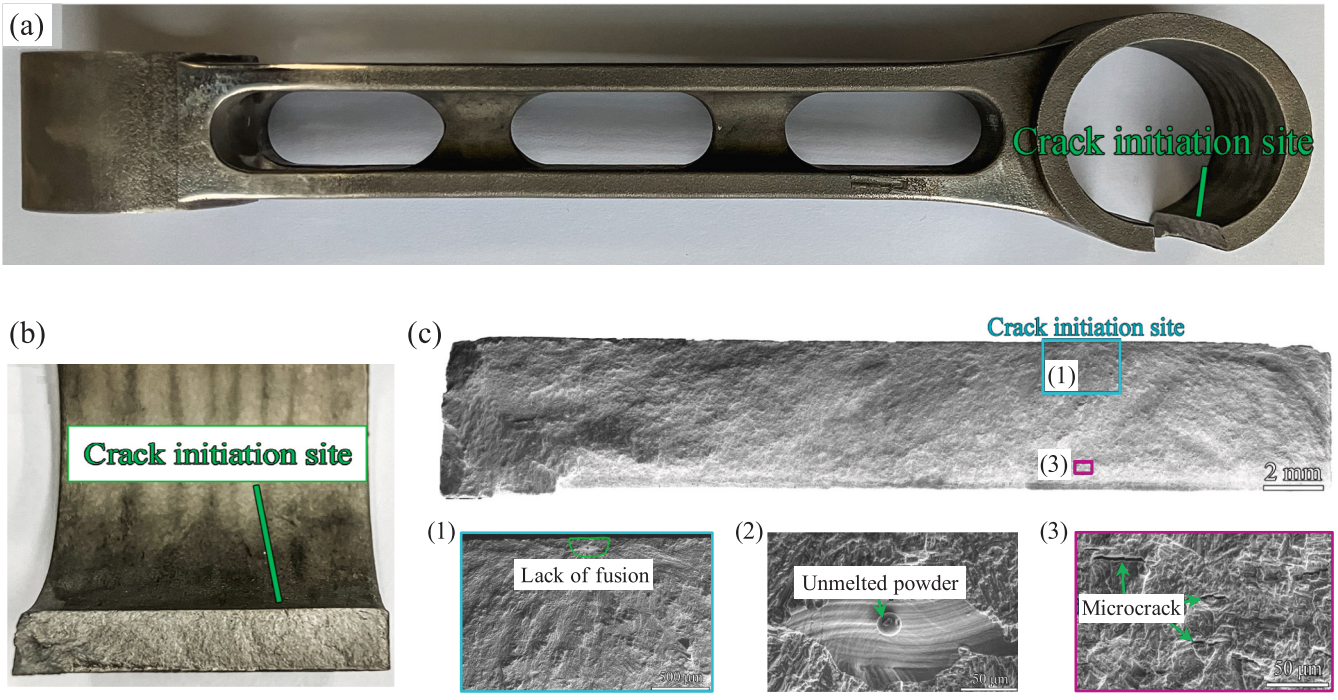

Fig. 12. (a) Physical photo of fracture location of non-HIP traction rod No.3 traction rod at 22.39 kN, 7.83 × 10^4 cycles. (b) is the enlarged image of the fracture location in (a). (c) SEM observation: (1) Magnified view of crack initiation site. (2) Magnified view of defect. (3) Enlarged view of the purple framed area in (a).

and 5.

Following HIP treatment, the fatigue fracture locations of the traction rods were still observed near the inner wall of the sleeve end, as shown in the physical image of the fractured HIP No.3 traction rod in Fig. 12(a) and Fig. 12(b). Further SEM observations of the fracture surface of the HIP No.3 traction rod are presented in Fig. 12(c). Interestingly, the "improvement" of defects in the traction rod due to HIP did not yield beneficial effects. The fatigue cracks in the HIP No.3 traction rod were single-origin and initiated from a large lack of fusion defect near the inner wall of the sleeve. The effective sizes of these defects were estimated using the green solid lines in Fig. 12(c-1). Unmelted powder was observed within the defects that induced crack initiation, as shown in Fig. 12(c-2). Additionally, numerous microcracks were detected in the crack propagation region near the outer wall of the sleeve, as shown in Fig. 12(c-3).

The fracture location of the HIP No.4 traction rod is shown in Fig. 13 (a) and (b). Similarly, the fracture occurred at the inner wall of the sleeve. SEM observations of the fracture surface revealed that the fatigue cracks had multiple origins, with two primary crack faces identified, as shown in Fig. 13(c). The crack initiation sites were located at single lack of fusion defects near the inner wall of the sleeve. These defects did not exhibit coalescence with adjacent surface defects. The effective defect sizes are indicated by green solid lines in Fig. 13(c-1) and (c-2). Defect 2, located near the edge of the sleeve wall, showed a high density of microcracks in the crack initiation, as shown in Fig. 13(c-3). Both defects exhibited highly irregular shapes, with sharp corners along their contours.

These observations indicate that, despite HIP treatment, significant AM process defects, including lack of fusion regions and unmelted powder, remained within the traction rods. Unlike material-level specimens, such structural-level complex components retain internal defects that cannot be effectively eliminated by HIP. On the contrary, the edges of internal defects became sharper after HIP, potentially causing further stress concentration and thereby adversely affecting fatigue performance.

Moreover, numerous studies have shown that surface roughness induces stress concentrations and thus degrades fatigue performance [34,74,75]. Murakami [72] proposed that the surface roughness produced by AM is larger and more detrimental than other defects and therefore cannot simply be treated as a small crack issue. To characterise the as-built surface condition of the AM Ti-6Al-4V traction rods, surface roughness was measured with a Zygo Nexview scanning white light interferometer. The original external surface was measured at mid part along the traction rod axis, while the sleeve inner wall was measured after fatigue failure, on the side surface near the fracture surface, starting at the bore centre and moving radially outward. The as-built external roughness differed little between the non-HIP and HIP rods, $Ra = 6.19$ μm and $Ra = 5.34$ μm, respectively, demonstrating that HIP does not improve the surface topography of structural components. After prolonged fatigue loading, friction between the rubber joints and the sleeve inner wall reduced the roughness to $Ra = 2.66$ μm (non-HIP) and $Ra = 2.40$ μm (HIP). These results indicate that the surface roughness at crack initiation sites actually decreases during service. Hence, surface roughness alone cannot fully describe the fatigue failure behaviour of the traction rods. The synergistic effects of multiple factors must be considered.

To further compare the differences between effective defect sizes and actual defect sizes, as well as the specific surface and interaction effects of adjacent defects, a quantitative analysis was conducted. Fig. 14 compares the effective and actual defect sizes of the crack initiating defects in Non-HIP material-level specimens and the four traction rods. The effective defect sizes in the figure were determined based on smoothed contour lines surrounding the original irregular defect shapes. The size distribution of crack-initiating defects in Non-HIP material-level specimens is marked by blue ellipses in Fig. 14. Detailed defect size information can be found in our previous work [47] and Table 3. For Non-HIP material-level specimens, the mean actual and effective defect sizes of crack-initiating defects were 53 μm and 59 μm, respectively. For the four traction rods, the mean actual and effective defect sizes were 87 μm and 137 μm, respectively. This indicates that both the actual and effective defect sizes of crack initiating defects in the material-level specimens were significantly smaller than those in the traction rods.

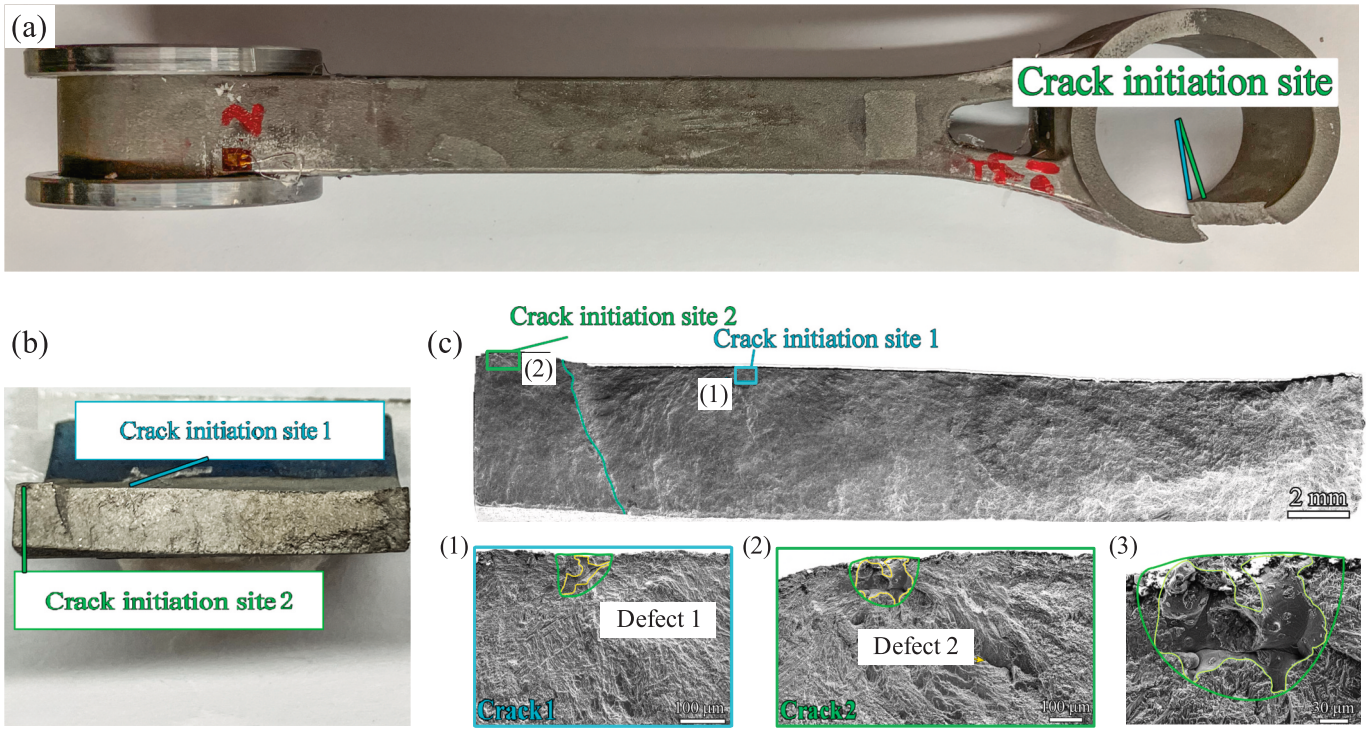

Fig. 13. (a) Physical photo of fracture location of non-HIP traction rod No.4 traction rod under 22.39 kN, 8.39×10^4 cycles. is the enlarged image of the fracture location in (a). (c) SEM observation: (1) Magnified view of crack initiation site 1. (2) Magnified view of crack initiation site 2. (3) Enlarged view of defect 2.

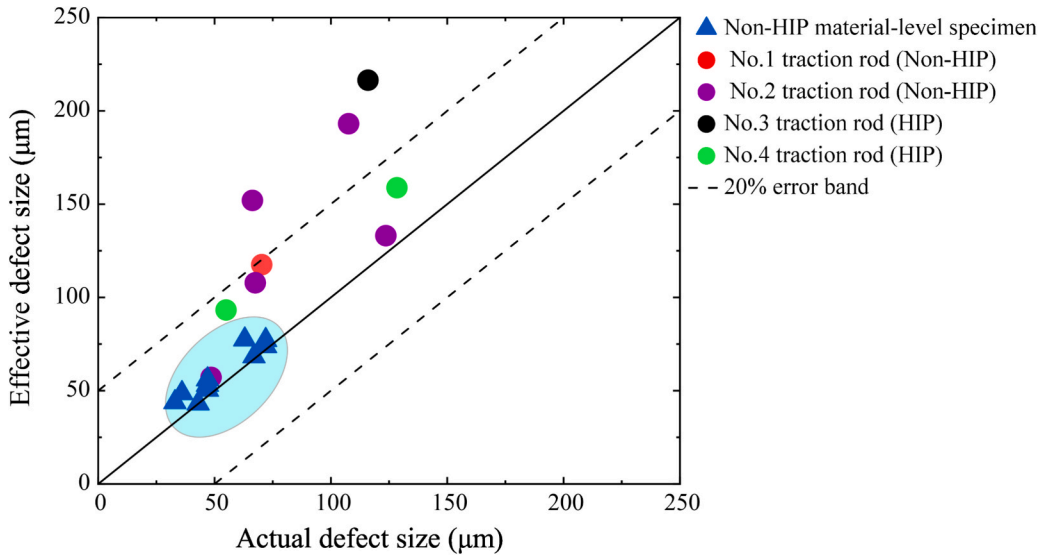

Fig. 14. Relationship between the effective and actual sizes of crack-initiating defects in ultrasonic frequency fatigue non-HIP material-level specimens and four traction rods.

Table 3
Traction rod test loads, lifetimes N_f, and the actual versus effective sizes of crack-initiating defects.

Specimen ID	Maximum load in fatigue test (kN)	Fatigue life (cycles)	Defect ID	$\sqrt{area}$(μm)	$\sqrt{area_{eff}}$(μm)	$\sqrt{area_{eff}}$Two-defect (μm)	$\sqrt{area_{eff}}$Three-defect (μm)
Non-HIP No.1	22.39	3.59×10^5	Defect 1	70	117	–	–
Non-HIP No.2	16.04	1.27×10^5	Defect 1	124	133	177	–
			Defect 2	49	57		–
			Defect 3	108	193	–	276
			Defect 4	66	152	190	
			Defect 5	68	108		
HIP No.3	22.39	7.83×10^4	Defect 1	116	216	–	–
HIP No.4	22.39	8.39×10^4	Defect 1	55	93	–	–
			Defect 2	128	159	–	–

Since the effective defect size is determined based on smoothed contour lines surrounding the original irregular defect shapes, it is inherently larger than the actual defect size. For internal defects in ultrasonic specimens, the mean ratio of effective defect size to actual defect size was 1.14, with a coefficient of variation of 10.57 %. However, for internal defects in traction rods, the mean ratio was 1.60, with a coefficient of variation of 22.68 %. This suggests that internal defects in traction rods exhibit more irregular shapes and being closer to the surface, surface defects are more harmful than subsurface or internal defects. Consequently, the effective defect size is generally greater than the actual size when evaluating surface defects [72].

These findings demonstrate that HIP treatment at the materials-level does not effectively mitigate AM process defects in structural components. As components become larger and more complex, the effectiveness of HIP in mitigating subsurface defects introduced by AM diminishes, especially for defects near the inner wall of the sleeve. Instead, the process compresses defects into more irregular shapes, resulting in larger effective defect sizes and adversely impacting fatigue performance.

4.4. Prediction of fatigue life from material to structural scale

HIP cannot effectively eliminate internal defects in structural components. Due to the challenges and high costs associated with structural testing, predicting structural fatigue life based on material-level data remains a widely accepted and practical approach. In this study, the explicit defects were not directly modelled. Instead, these defects were represented as virtual cracks by constructing an envelope crack geometry that bounds the observed defect morphology. This envelope serves as the initial crack shape for the subsequent crack propagation analysis. By treating such defects as initial cracks—whose size and geometry are based on fractographic observations—their influence on fatigue performance is indirectly accounted. This approach allows the model to conservatively estimate fatigue life and is particularly useful when dealing with small or irregular flaws that act as dominant crack initiation sites but are difficult to model explicitly. This approach is implemented through the following three steps:

(1) *Defect Characterization*: The irregular defect is approximated as a semi-elliptical shape with a width W_d and depth a_d, as depicted in Fig. 15(a).
(2) *Virtual Crack Assumption*: The semi-elliptical defect is treated as a virtual crack. The fatigue life consumed by this virtual crack, denoted as N_d, corresponds to the crack depth a_d on the *N-a* curve derived from the multiscale fatigue model without defects (represented by the red curve in Fig. 15(b)).
(3) *Fatigue Life Adjustment*: The total fatigue life of the rods, incorporating the effect of defects, is determined as the remaining fatigue life after the virtual crack stage, given by $N_r = N_f - N_d$. This is represented by the green curve in Fig. 15(b).

By analysing the defects observed in the SEM images (Figs. 12 and 13), the average depth of the virtual cracks was determined to be a_d = 132.8μm. A comparison of the predicted *S-N* curves, both with and

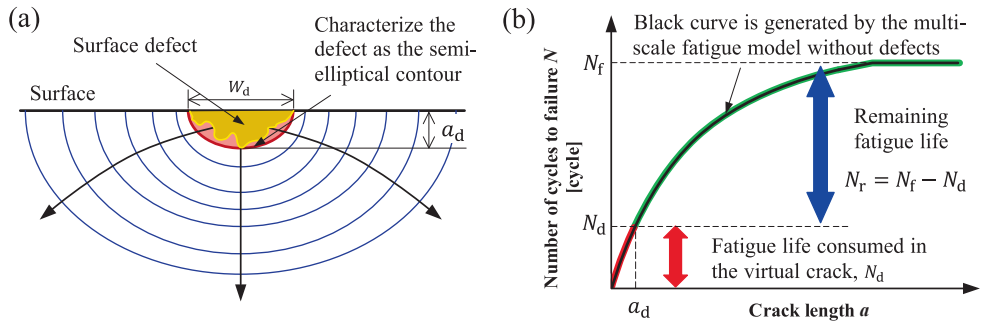

Fig. 15. Treatment for considering the effect of defects: (a) defect characterization and (b) fatigue life adjustment.

without defects, with the experimental results is presented in Fig. 16. The experimental data falls between the predicted values, i.e., N_f and N_r, indicating that the proposed prediction model exhibits good accuracy in covering the experimental results.

Although the predicted fatigue life considering virtual cracks is slightly lower than the experimental values, this discrepancy can be explained as follows. In practice, fatigue cracks initiate from defects (outlined in yellow in Fig. 15(a)) at a relatively low growth rate. However, in our approach, the fatigue life is considered as the remaining life starting from the initial virtual crack, implying that the crack has already reached a higher growth rate at the outset, i.e., $a = a_d$. As a result, the predicted remaining fatigue life is shorter than the actual values. This discrepancy will be reduced in future studies by optimizing the modelling approach.

Furthermore, the model successfully estimated the fatigue limit of the traction rod, which was determined to be 500 MPa, demonstrating its capability to provide accurate fatigue life assessments for structural components.

5. Conclusions

This study experimentally investigated the fatigue behaviour of an additively manufactured Ti-6Al-4V traction rod, specifically designed for high-speed railway applications, and compared it with that of material-level specimens. To capture microstructural grain-boundary interactions in the hexagonal close-packed titanium alloy, a multiscale fatigue modelling strategy was developed, offering a novel approach for characterising crack growth in AM Ti-6Al-4V components. The main findings can be summarised as follows:

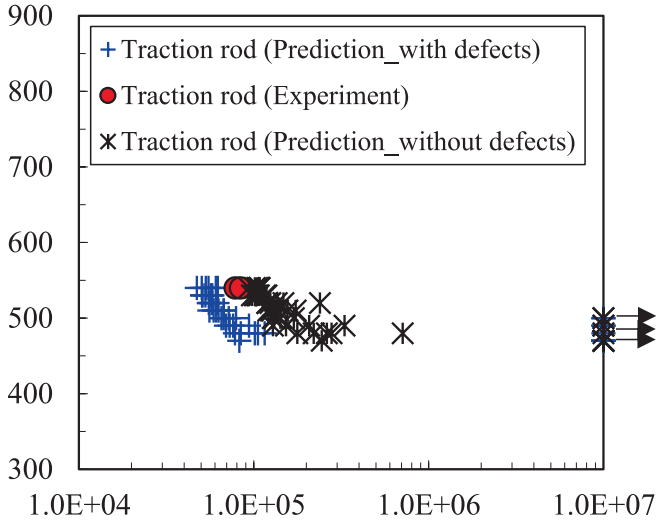

Fig. 16. Predicted *S-N* curves of traction rods with experimental validation and estimated fatigue limit.

1. Through topology optimisation and selective laser melting, the traction rod achieved a 66.74 % weight reduction while meeting load-bearing requirements. Although HIP effectively removed small internal pores in material-level coupons, it did not eliminate larger near surface lack of fusion defects in the traction rod; moreover, the edges of these defects became even sharper after HIP, causing intensified local stress concentrations. Consequently, the fatigue performance of traction rod showed no improvement and even deteriorated at the structural scale, where multiple large surface defects acted as dominant crack initiation sites.
2. HIP leaves the as-built surface essentially unchanged, yet surface roughness alone cannot predict fatigue behaviour, which is governed by the coupled action of surface and subsurface defects. For defect sensitive AM structures, the notion of "effective defect size" provided more conservative and accurate assessments of irregular defect morphologies, particularly near the surface where local stresses were significantly magnified.
3. The integrated multiscale modelling approach, combining macro-scale FEA with micro-scale grain boundary interactions, accurately captured fatigue crack growth in AM alloys, underscoring the importance of microstructure-informed prediction methods for complex metallic systems.
4. The newly developed multiscale model was successfully extended to hexagonal close-packed Ti-6Al-4V, broadening its applicability beyond ferrite-based steels and demonstrating its capability to handle more intricate crystal structures.
5. Validation using both coupon-level and traction-rod fatigue tests confirmed the predictive accuracy of the model. Notably, the predicted fatigue limit of 500 MPa for the traction rod closely matches experimental observations, highlighting the model's reliability for real-world engineering applications.

Overall, these findings underscore the critical influence of manufacturing-induced defects on the fatigue performance of AM Ti-6Al-4V, and demonstrate that a multiscale, microstructure-informed approach is essential for achieving accurate, cost-effective fatigue life predictions in complex engineering structures.

CRediT authorship contribution statement

Weiqian Chi: Writing – review & editing, Writing – original draft, Methodology, Investigation, Formal analysis, Data curation, Conceptualization. **Wenjing Wang:** Writing – review & editing, Validation, Supervision, Project administration, Methodology, Investigation, Funding acquisition, Formal analysis. **Hongchang Zhou:** Writing – review & editing, Writing – original draft, Visualization, Methodology, Funding acquisition, Formal analysis, Conceptualization. **Ruiguo Yan:** Writing – review & editing. **Yoshiki Mikami:** Writing – review & editing, Supervision, Resources, Funding acquisition, Formal analysis.

Declaration of competing interest

The authors declare that they have no known competing financial interests or personal relationships that could have appeared to influence the work reported in this paper.

Acknowledgement

The authors acknowledge the support of the National Natural Science Foundation of China (12402087, U2468209), the Science and Technology Research and Development Program of China State Railway Group Co., Ltd. (P2024J001), and the China Scholarship Council (CSC). This work was partly supported by JSPS KAKENHI (24 K22929, 24 K00967). Authors appreciate the support by OU Master Plan Implementation Project, The University of Osaka on this research work.

Appendix A

In Section 3.4.1, σ_{max} represents the maximum applied stress, while σ_{op} denotes the crack opening stress. Their respective formulations are as follows [67]:

$$\sigma_{max} = \frac{2}{1-R}\sigma_{yy}^{eff}[\sigma_{nom}, a],$$

$$\sigma_{op} = -\left(\sigma_a + \sigma_{op}^{\infty}\right)\exp(-0.028b) + \sigma_{op}^{\infty},$$

$$\sigma_{op}^{\infty} = \left(A_0 + A_1 R + A_2 R^2 + A_3 R^3\right)\sigma_{max},$$

$$A_0 = \left(0.825 - 0.34\alpha + 0.05\alpha^2\right)\cos\left(\frac{\pi\sigma_{max}}{\sigma_Y + \sigma_B}\right)^{1/\alpha},$$

$$A_1 = (0.415 - 0.071\alpha)\frac{2\sigma_{max}}{\sigma_Y + \sigma_B},$$

$$A_2 = 1 - A_0 - A_1 - A_3,$$

$$A_3 = 2A_0 + A_1 - 1, \tag{A.1}$$

where σ_{op}^{∞} represents the crack opening stress for a long crack, as proposed by Newman [76]. The parameter R is the applied stress ratio, while σ_Y and σ_B correspond to the monotonic yield strength and ultimate tensile strength, respectively. The constraint factor α s assumed to be 3 under plane strain conditions. The term σ_{yy}^{eff} represents the normal component of the uniform remote stress σ_{eff}. Based on the crack/GB interaction theory, σ_{eff} defined as the uniform remote stress applied to a 2D crack. This ensures that the stress intensity factor K at the deepest point of the crack is equivalent to that generated by the actual applied stress σ_{eq} in a 3D body, as illustrated in Fig. A.1.

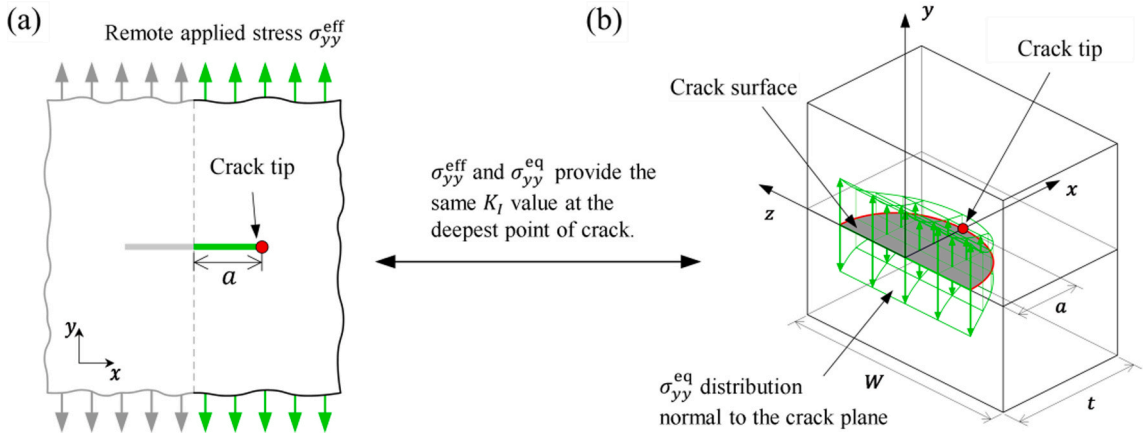

Fig. A1. Illustration of the equivalent effect of and , which yield the K at crack depth a for 2D and 3D cracks. Here, and denote the normal components of and in the loading direction, respectively.

In Eq. (A.1), σ_{eq} is formulated based on the relative elastic and plastic strain tensors from the macroscopic FE analysis in Sections 3.2, and is given by [67]:

$$\sigma_{eq}[\sigma_{nom}] = \mathbf{C}_e : \varepsilon_e[\sigma_{nom}] + \mathbf{C}_p : \varepsilon_p[\sigma_{nom}], \tag{A.2}$$

where $\mathbf{C}_e$ and $\mathbf{C}_p$ represent elastic and plastic coefficient tensors, respectively, with Poisson's ratios assumed to be $\nu = 0.3$ for the elastic case and $\nu = 0.5$, for the plastic case.

In Fig. A.1 (a), the stress intensity factor K for a crack in an infinite plate subjected to uniform tensile stress is expressed as a function of the nominal stress σ_{nom} and crack depth a, given by:

$$K[\sigma_{\text{nom}}, a] = \sigma_{yy}^{\text{eff}}[\sigma_{\text{nom}}, a]\sqrt{\pi a}. \tag{A.3}$$

In Fig. A.1 (b), the stress intensity factor K for a 3D cracked body with a thickness t, width W, and a semi-elliptical crack of depth a and aspect ratio r is determined using the following equation:

$$K[\sigma_{\text{nom}}, a] = \int_0^a \left(\sigma_{yy}^{\text{eq}}[\sigma_{\text{nom}}, x] \bullet m[x, a, r, t, W]\right) dx, \tag{A.4}$$

$$m[x, a, r, t, W] = M_1 + M_2\left(1 - \frac{x}{a}\right)^{-\frac{1}{2}} + M_3\left(1 - \frac{x}{a}\right)^{\frac{1}{2}} + M_4\left(1 - \frac{x}{a}\right), \tag{A.5}$$

where m represents a weight function defined by four parameters (M_1, M_2, M_3 and M_4). These parameters are determined through a systematic FE analysis. A detailed derivation of their solutions can be found in [62].

By substituting Eq. (A.3) into Eq. (A.2), we obtain σ_{yy}^{eff} as expressed by σ_{yy}^{eq}:

$$\sigma_{yy}^{\text{eff}}[\sigma_{\text{nom}}, a] = \frac{\int_0^a \left(\sigma_{yy}^{\text{eq}}[\sigma_{\text{nom}}, x] \bullet m[x, a, r, t, W]\right) dx}{\sqrt{\pi a}}. \tag{A.6}$$

Assuming that σ_{eff} and σ_{eq} have the same relationship as σ_{yy}^{eff} and σ_{yy}^{eq} in Eq. (A.5), σ_{eff} is thus given by:

$$\sigma_{\text{eff}}[\sigma_{\text{nom}}, a] = \frac{\int_0^a \left(\sigma_{\text{eq}}[\sigma_{\text{nom}}, x] \bullet m[x, a, r, t, W]\right) dx}{\sqrt{\pi a}}. \tag{A.7}$$

Appendix B

Steel A, a ferrite-pearlite steel from our previous research [68], has its chemical composition, tensile properties, and microstructural characteristics detailed in Tables B.1 and B.2, respectively.

Fig. B.1a presents its optical micrograph, while Fig. B.1b displays the inverse pole figure (IPF) map. Fig. B.1c illustrates the distributions of pearlite band thicknesses and the equivalent diameters of ferrite grains. Three-point bending test specimens were machined from Steel A, with their geometrical configuration shown in Fig. B.1d. Fatigue tests were carried out using these specimens at a loading frequency of 20 Hz and a stress ratio of R = 0.1, as depicted in Fig. B.1e. The constants for the crack growth law in Eq. (6) were identified by fitting the simulated results with the experimental data for Steel A. The determined values are $C = 15.5$, $n = 1.8$, and $\Delta CTSD_{\text{th}} = 1.12 \times 10^{-4}$mm, as illustrated in Fig. B.2.

Table B1
Chemical compositions of steel A.

Steel	C	Si	Mn	P	S	Al	N
A	0.18	0.15	1.00	<0.002	0.0005	0.019	0.0008

Table B2 The tensile properties and microstructural information of steel A.

Monotonic yield strength [MPa]	Cyclic yield strength [MPa]	Tensile strength [MPa]	Reduction in area [-]	Average grain size [μm]	Friction strength to move dislocations [MPa]	
					Ferrite	Pearlite
216	285	430	0.72	56.6	62.3	86.8

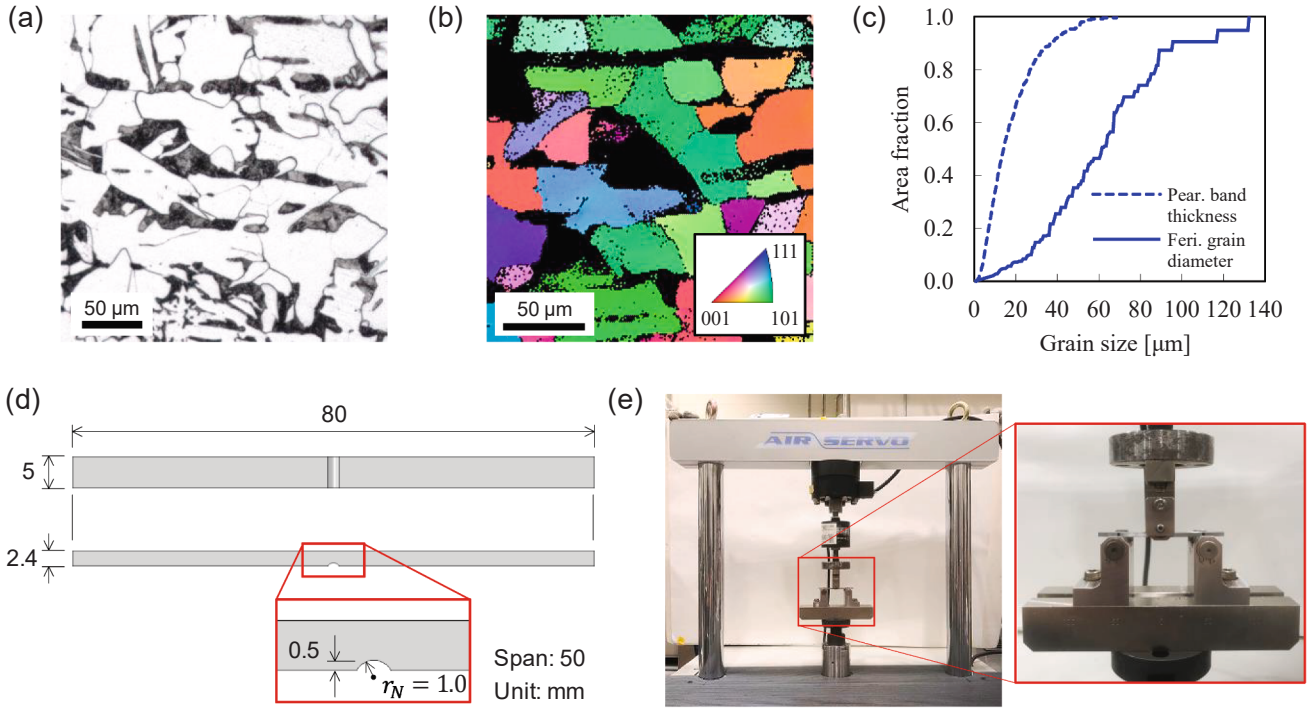

Fig. B1. Microstructural characteristics of Steel A and fatigue testing setup: (a) optical micrograph, (b) IPF map from EBSD analysis, (c) distribution of pearlite band thicknesses and ferrite grain equivalent diameters, (d) specimen geometry, and (e) fatigue test setup.

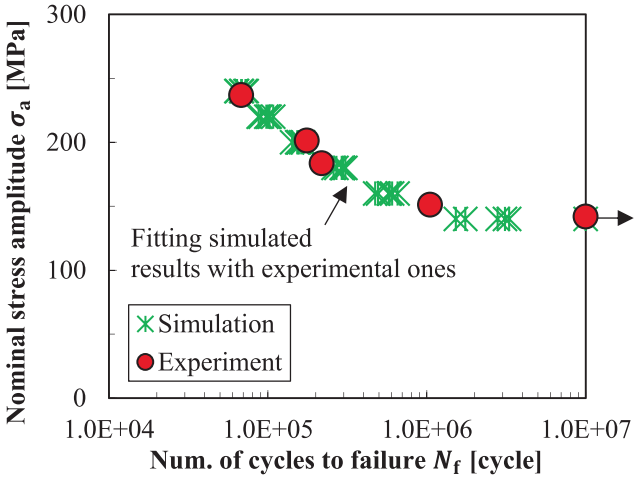

Fig. B2. Identification of the crack growth law's constants in Eq. (6).

Data availability

Data will be made available on request.

References

[1] Su J, Jiang F, Teng J, Chen L, Yan M, Requena G, et al. Recent innovations in laser additive manufacturing of titanium alloys. Int J Extrem Manuf 2024;6:032001. https://doi.org/10.1088/2631-7990/ad2545.
[2] Liang J, Wu D, Liu S, Wang H, Yu J. Research on hybrid remanufacturing process chain of laser cladding, CNC machining and ultrasonic rolling for aero-engine blades. J Manuf Process 2024;110:331–49. https://doi.org/10.1016/j.jmapro.2023.12.059.
[3] Cao Z, Cui L, Luo S, Su H, Pang Z, Zhao W, et al. Superior fretting wear resistance of titanium alloys from stable gradient nanostructures induced by laser shock peening. Int J Plast 2025;188:104293. https://doi.org/10.1016/j.ijplas.2025.104293.
[4] Li Y, Chen H, Du L, Yang F, Zhang Y, Li D. Characterization and unified modelling of creep and viscoplasticity deformation of titanium alloy at elevated temperature. Int J Plast 2024;173:103892. https://doi.org/10.1016/j.ijplas.2024.103892.
[5] Zhao G, Zhao B, Ding W, Xin L, Nian Z, Peng J, et al. Nontraditional energy-assisted mechanical machining of difficult-to-cut materials and components in aerospace community: a comparative analysis. Int J Extrem Manuf 2024;6:022007. https://doi.org/10.1088/2631-7990/ad16d6.
[6] Liu S, Shin YC. Additive manufacturing of Ti6Al4V alloy: a review. Mater Des 2019;164:107552. https://doi.org/10.1016/j.matdes.2018.107552.
[7] Liu G, Zhang X, Chen X, He Y, Cheng L, Huo M, et al. Additive manufacturing of structural materials. Mater Sci Eng R Rep 2021;100596. https://doi.org/10.1016/j.mser.2020.100596.
[8] Herzog D, Seyda V, Wycisk E, Emmelmann C. Additive manufacturing of metals. Acta Mater 2016;117:371–92. https://doi.org/10.1016/j.actamat.2016.07.019.

[9] Zhang Z, Yang B, Xiao S. Revolutionizing rail transportation: unleashing titanium alloys for enhanced performance, safety, and sustainability. Chin J Mech Eng 2025; 38:72. https://doi.org/10.1186/s10033-025-01229-3.

[10] Miwa M, Kawasaki Y, Yoshimura A. Influence of vehicle unsprung-mass on dynamic wheel load. WIT Trans Built Environ 2008;103:715–24.

[11] Zhang Z, Xu Z. Fatigue database of additively manufactured alloys. Sci Data 2023; 10:249. https://doi.org/10.1038/s41597-023-02150-x.

[12] Chern AH, Nandwana P, Yuan T, Kirka MM, Dehoff RR, Liaw PK, et al. A review on the fatigue behavior of Ti-6Al-4V fabricated by electron beam melting additive manufacturing. Int J Fatigue 2019;119:173–84. https://doi.org/10.1016/j.ijfatigue.2018.09.022.

[13] Sun X, Chen M, Liu T, Zhang K, Wei H, Zhu Z, et al. Characterization, preparation, and reuse of metallic powders for laser powder bed fusion: a review. Int J Extrem Manuf 2024;6:012003. https://doi.org/10.1088/2631-7990/acfbc3.

[14] Razavi N, Askes H, Berto F, Susmel L. Length scale parameters to estimate fatigue lifetime of 3D-printed titanium alloy Ti6Al4V containing notches in the as-manufactured condition. Int J Fatigue 2023;167:107348. https://doi.org/10.1016/j.ijfatigue.2022.107348.

[15] Le VD, Pessard E, Morel F, Prigent S. Fatigue behaviour of additively manufactured Ti-6Al-4V alloy: the role of defects on scatter and statistical size effect. Int J Fatigue 2020;140:105811. https://doi.org/10.1016/j.ijfatigue.2020.105811.

[16] Wang YW, Yu K, Pan Y, Zhu YC, Wang JY, Jiang L, et al. Microstructure evolution and mechanical properties of GH3535 alloy produced by wire arc additive manufacturing. Mater Sci Eng A 2025;923:147667. https://doi.org/10.1016/j.msea.2024.147667.

[17] Sanaei N, Fatemi A. Defects in additive manufactured metals and their effect on fatigue performance: a state-of-the-art review. Prog Mater Sci 2021;117:100724. https://doi.org/10.1016/j.pmatsci.2020.100724.

[18] Becker TH, Kumar P, Ramamurty U. Fracture and fatigue in additively manufactured metals. Acta Mater 2021;219:117240. https://doi.org/10.1016/j.actamat.2021.117240.

[19] DebRoy T, Wei HL, Zuback JS, Mukherjee T, Elmer JW, Milewski JO, et al. Additive manufacturing of metallic components–process, structure and properties. Prog Mater Sci 2018;92:112–224. https://doi.org/10.1016/j.pmatsci.2017.10.001.

[20] Moran TP, Carrion PE, Lee S, Shamsaei N, Phan N, Warner DH. Hot isostatic pressing for fatigue critical additively manufactured Ti-6Al-4V. Mater 2022;15: 2051. https://doi.org/10.3390/ma15062051.

[21] Jesus JS, Borrego LP, Ferreira JAM, Costa JD, Batista AC, Capela C. Fatigue crack growth in Ti-6Al-4V specimens produced by laser powder bed fusion and submitted to hot isostatic pressing. Theor Appl Fract Mech 2022;118:103231. https://doi.org/10.1016/j.tafmec.2021.103231.

[22] Guennec B, Hattal A, Hocini A, Mukhtarova K, Kinoshita T, Horikawa N, et al. Fatigue performance of zirconia-reinforced Ti-6Al-4V nanocomposite processed by laser powder bed fusion: an improvement by hot isostatic pressing. Int J Fatigue 2022;164:107129. https://doi.org/10.1016/j.ijfatigue.2022.107129.

[23] Xi J, Hu Y, Xing H, Han Y, Zhang H, Jiang J, et al. The low-cycle fatigue behavior, failure mechanism and prediction of SLM Ti-6Al-4V alloy with different heat treatment methods. Mater 2021;14:6276. https://doi.org/10.3390/ma14216276.

[24] Yu H, Li F, Wang Z, Zeng X. Fatigue performances of selective laser melted Ti-6Al-4V alloy: influence of surface finishing, hot isostatic pressing and heat treatments. Int J Fatigue 2019;120:175–83. https://doi.org/10.1016/j.ijfatigue.2018.11.019.

[25] Li P, Warner DH, Pegues JW, Roach MD, Shamsaei N, Phan N. Investigation of the mechanisms by which hot isostatic pressing improves the fatigue performance of powder bed fused Ti-6Al-4V. Int J Fatigue 2019;120:342–52. https://doi.org/10.1016/j.ijfatigue.2018.10.015.

[26] Molaei R, Fatemi A, Phan N. Significance of hot isostatic pressing (HIP) on multiaxial deformation and fatigue behaviors of additive manufactured Ti-6Al-4V including build orientation and surface roughness effects. Int J Fatigue 2018;117: 352–70. https://doi.org/10.1016/j.ijfatigue.2018.07.035.

[27] Derimow N, Benzing JT, Newton D, Beamer C, Lu P, DelRio FW, et al. Microstructural effects on the rotating bending fatigue behavior of Ti-6Al-4V produced via laser powder bed fusion with novel heat treatments. Int J Fatigue 2024;185:108362. https://doi.org/10.1016/j.ijfatigue.2024.108362.

[28] Günther J, Krewerth D, Lippmann T, Leuders S, Tröster T, Weidner A, et al. Fatigue life of additively manufactured Ti–6Al–4V in the very high cycle fatigue regime. Int J Fatigue 2017;94:236–45. https://doi.org/10.1016/j.ijfatigue.2016.05.018.

[29] Greitemeier D, Palm F, Syassen F, Melz T. Fatigue performance of additive manufactured TiAl6V4 using electron and laser beam melting. Int J Fatigue 2017; 94:211–7. https://doi.org/10.1016/j.ijfatigue.2016.05.001.

[30] Benmessaoud F, Cheikh M, Velay V, Vidal V, Matsumoto H. Role of grain size and crystallographic texture on tensile behavior induced by sliding mechanism in Ti-6Al-4V alloy. Mater Sci Eng A 2020;774:138835. https://doi.org/10.1016/j.msea.2019.138835.

[31] Cordero ZC, Knight BE, Schuh CA. Six decades of the Hall-Petch effect- a survey of grain-size strengthening studies on pure metals. Int Mater Rev 2016;61:495–512. https://doi.org/10.1080/09506608.2016.1191808.

[32] Benzing J, Hrabe N, Quinn T, White R, Rentz R, Ahlfors M. Hot isostatic pressing (HIP) to achieve isotropic microstructure and retain as-built strength in an additive manufacturing titanium alloy (Ti-6Al-4V). Mater Lett 2019;257:126690. https://doi.org/10.1016/j.matlet.2019.126690.

[33] Liu TY, Shi K, Zhao J, Liu SB, Zhang YW, Liu HY, et al. Effect of hot isostatic pressing processing parameters on microstructure and properties of Ti60 high temperature titanium alloy. China Foundry 2023;20:49–56. https://doi.org/10.1007/s41230-022-2070-6.

[34] Leuders S, Meiners S, Wu L, Taube A, Tröster T, Niendorf T. Structural components manufactured by Selective Laser Melting and Investment Casting-Impact of the process route on the damage mechanism under cyclic loading. J Mater Process Technol 2017;248:130–42. https://doi.org/10.1016/j.jmatprotec.2017.04.026.

[35] Romano S, Brandão A, Gumpinger J, Gschweitl M, Beretta S. Qualification of AM parts: Extreme value statistics applied to tomographic measurements. Mater Des 2017;131:32–48. https://doi.org/10.1016/j.matdes.2017.05.091.

[36] Portolés L, Jordá O, Jordá L, Uriondo A, Esperon-Miguez M, Perinpanayagam S. A qualification procedure to manufacture and repair aerospace parts with electron beam melting. J Manuf Syst 2016;41:65–75. https://doi.org/10.1016/j.jmsy.2016.07.002.

[37] Gorelik M. Additive manufacturing in the context of structural integrity. Int J Fatigue 2017;94:168–77. https://doi.org/10.1016/j.ijfatigue.2016.07.005.

[38] Li P, Warner DH, Phan N. Predicting the fatigue performance of an additively manufactured Ti-6Al-4V component from witness coupon behavior. Addit Manuf 2020;35:101230. https://doi.org/10.1016/j.addma.2020.101230.

[39] Kasprzak JM, Lass AB, Miller CE. Development, test, and evaluation of additively manufactured flight critical aircraft components. AHS Int 73rd Annu Forum Technol Display. 2017.

[40] Wu Z, Wu S, Qian W, Zhang H, Zhu H, Chen Q, et al. Structural integrity issues of additively manufactured railway components: progress and challenges. Eng Fail Anal 2023;149:107265. https://doi.org/10.1016/j.engfailanal.2023.107265.

[41] Pei X, Dong P, Kim MH. A simplified structural strain method for low-cycle fatigue evaluation of girth-welded pipe components. Int J Fatigue 2020;139:105732. https://doi.org/10.1016/j.ijfatigue.2020.105732.

[42] Liang Z, Wang XS, Cui YN, Xu W, Zhang Y, He YH. A new data-driven probabilistic fatigue life prediction framework informed by experiments and multiscale simulation. Int J Fatigue 2023;174:107731. https://doi.org/10.1016/j.ijfatigue.2023.107731.

[43] Song K, Wang K, Zhao L, Xu L, Ma N, Han Y, et al. A physically-based constitutive model for a novel heat resistant martensitic steel under different cyclic loading modes: Microstructural strengthening mechanisms. Int J Plast 2023;165:103611. https://doi.org/10.1016/j.ijplas.2023.103611.

[44] Song K, Xu L, Zhao L, Han Y, Ma N, Wang K, et al. Effect of loading modes on uniaxial creep-fatigue deformation: a dislocation based viscoplastic constitutive model. Int J Plast 2024;179:104038. https://doi.org/10.1016/j.ijplas.2024.104038.

[45] Hu C, Xu L, Zhao L, Han Y, Song K, Luo X, et al. Investigation of low cycle fatigue crack propagation behavior of 316H steel at 550℃ based on cyclic response and damage accumulation: experiment and modelling. Int J Plast 2023;167:103661. https://doi.org/10.1016/j.ijplas.2023.103661.

[46] Shibanuma K, Ueda K, Ito H, Nemoto Y, Kinefuchi M, Enoki M. Model for predicting fatigue life and limit of steels based on micromechanics of small crack growth. Mater Des 2018;139:269–82. https://doi.org/10.1016/j.matdes.2017.10.069.

[47] Chi W, Wang W, Li Y, Xu W, Sun C. Defect induced cracking and modeling of fatigue strength for an additively manufactured Ti-6Al-4V alloy in very high cycle fatigue regime. Theor Appl Fract Mech 2022;119:103380. https://doi.org/10.1016/j.tafmec.2022.103380.

[48] Tridello A, Fiocchi J, Biffi C, Chiandussi G, Rossetto M, Tuissi A, et al. VHCF response of heat-treated SLM Ti6Al4V Gaussian specimens with large loaded volume. Procedia Struct Integr 2019;18:314–21. https://doi.org/10.1016/j.prostr.2019.08.171.

[49] Xue G, Nakamura T, Fujimura N, Takahashi K, Oguma H, Takeuchi A, et al. Initiation and propagation of small fatigue crack in beta titanium alloy observed through synchrotron radiation multiscale computed tomography. Eng Fract Mech 2022;263:108308. https://doi.org/10.1016/j.engfracmech.2022.108308.

[50] Zhou H, Kinefuchi M, Takashima Y, Shibanuma K. Multiscale modelling strategy for predicting fatigue performance of welded joints. Int J Mech Sci 2024;284: 109751. https://doi.org/10.1016/j.ijmecsci.2024.109751.

[51] Zhou H, Liu Z, Kikuchi S, Shibanuma K. Analysis of fatigue performance of austenitic stainless steels with bimodal harmonic structures based on multiscale model simulations. Mater Des 2023;226:111657. https://doi.org/10.1016/j.matdes.2023.111657.

[52] Li J, Sun Q, Zhang ZP, Li CW, Qiao YJ. Theoretical estimation to the cyclic yield strength and fatigue limit for alloy steels. Mech Res Commun 2009;36:316–21. https://doi.org/10.1016/j.mechrescom.2008.10.011.

[53] Li J, Zhang Z, Li C. An improved method for estimation of Ramberg-Osgood curves of steels from monotonic tensile properties. Fatigue Fract Eng Mater Struct 2016; 39:412–26. https://doi.org/10.1111/ffe.12366.

[54] Masing G. Eigenspannungen und verfestigung beim messing 1935:332–5. in German.

[55] Wright SI. A review of automated orientation imaging microscopy (OIM). J Comput Assist Microsc 1993;5:207–21.

[56] Ju Y, Zhang Y, Yu H. Numerical prediction and experiments for 3D crack propagation in brittle materials based on 3D-generalized maximum tangential strain criterion. Theor Appl Fract Mech 2025;135:104747. https://doi.org/10.1016/j.tafmec.2024.104747.

[57] Yan RG, Wang WJ, Zhou PY, Shan W. Research on monitoring method for crack depth of railway hollow axle during bench test. Fatigue Fract Eng Mater Struct 2023;46:4649–62. https://doi.org/10.1111/ffe.14151.

[58] Yan R-G, Wang W-J, Ding R, Zeng Y-M, Shan W, Yin Y, et al. Research on size effects in fracture properties and residual life prediction for high-speed train axles. Theor Appl Fract Mech 2024;134:104715. https://doi.org/10.1016/j.tafmec.2024.104715.

[59] Zhou P, Zhou J, Ye Z, Hong X, Huang H, Xu W. Effect of grain size and misorientation angle on fatigue crack growth of nanocrystalline materials. Mater Sci Eng A 2016;663:1–7. https://doi.org/10.1016/j.msea.2016.03.105.

[60] Tanaka K, Akiniwa Y, Nakai Y, Wei RP. Modelling of small fatigue crack growth interacting with grain boundary. Eng Fract Mech 1986;24:803–19. https://doi.org/10.1016/0013-7944(86)90266-3.
[61] Mura T. Continuous distribution of moving dislocations. Phil Mag 1963;8:843–57. https://doi.org/10.1080/14786436308213841.
[62] Zhou H, Suzuki Y, Kinefuchi M, Schmauder S, Dogahe K, Shibanuma K. Bridging strategy between microscopic and macroscopic crack growth simulations to predict fatigue strength of steels. Int J Fatigue 2023;168:107386. https://doi.org/10.1016/j.ijfatigue.2022.107386.
[63] Bang D, Ince A, Noban M. Modeling approach for a unified crack growth model in short and long fatigue crack regimes. Int J Fatigue 2019;128:105182. https://doi.org/10.1016/j.ijfatigue.2019.06.042.
[64] Schaef W, Marx M. A numerical description of short fatigue cracks interacting with grain boundaries. Acta Mater 2012;60:2425–36. https://doi.org/10.1016/j.actamat.2012.01.013.
[65] Gu Y, Stiles CD, El-Awady JA. A statistical perspective for predicting the strength of metals: Revisiting the Hall-Petch relationship using machine learning. Acta Mater 2024;266:119631. https://doi.org/10.1016/j.actamat.2023.119631.
[66] Smith WF, Hashemi J, Presuel-Moreno F. Foundations of materials science and engineering. New York: McGraw-Hill; 2006.
[67] Ito H, Suzuki Y, Nishikawa H, Kinefuchi M, Enoki M, Shibanuma K. Multiscale model prediction of ferritic steel fatigue strength based on microstructural information, tensile properties, and loading conditions (no adjustable material constants). Int J Mech Sci 2020;170:105339. https://doi.org/10.1016/j.ijmecsci.2019.105339.
[68] Zhou H, Liu Z, Kinefuchi M, Shibanuma K. Multiscale modelling strategy for predicting fatigue lives and limits of steels based on a generalised evaluation method of grain boundaries effects. Int J Fatigue 2022;158:106749. https://doi.org/10.1016/j.ijfatigue.2022.106749.
[69] En,. 13749: Railway applications – Wheelsets and bogies – Method of specifying the structural requirements of bogie frames. Brussels: CEN; 2011.
[70] Murakami Y. Metal fatigue: effects of small defects and nonmetallic inclusions. Oxford: Academic Press; 2019.
[71] Murakami Y, Nemat-Nasser S. Growth and stability of interacting surface flaws of arbitrary shape. Eng Fract Mech 1983;17:193–210. https://doi.org/10.1016/0013-7944(83)90027-9.
[72] Masuo H, Tanaka Y, Morokoshi S, Yagura H, Uchida T, Yamamoto Y, et al. Influence of defects, surface roughness and HIP on the fatigue strength of Ti-6Al-4V manufactured by additive manufacturing. Int J Fatigue 2018;117:163–79. https://doi.org/10.1016/j.ijfatigue.2018.07.020.
[73] Murakami Y, Endo M. Effects of hardness and crack geometries on ΔK_{th} of small cracks emanating from small defects. 1986.
[74] Fu R, Zheng L, Zhong Z, Hong Y. High-cycle and very-high-cycle fatigue behavior at two stress ratios of Ti-6Al-4V manufactured via laser powder bed fusion with different surface states. Fatigue Fract Eng Mater Struct 2023;46:2348–63. https://doi.org/10.1111/ffe.13985.
[75] Shrestha R, Simsiriwong J, Shamsaei N. Fatigue behavior of additive manufactured 316L stainless steel under axial versus rotating-bending loading: synergistic effects of stress gradient, surface roughness, and volumetric defects. Int J Fatigue 2021;144:106063. https://doi.org/10.1016/j.ijfatigue.2020.106063.
[76] Newman JC. A crack opening stress equation for fatigue crack growth. Int J Fract 1984;24:131–5. https://doi.org/10.1007/BF00020751.